A hysteretic model for fiber-reinforced composites at finite strains: fractional derivatives, computational aspects and analysis

Yvan Denis, Fabrice Morestin, Nahiene Hamila

A hysteretic model for fiber-reinforced composites at finite strains: fractional derivatives, computational aspects and analysis

Yvan Denis[a], Fabrice Morestin[a], Nahiene Hamila[a,*]

[a] *Université de Lyon, INSA-Lyon, LaMCoS, CNRS UMR 5259, F-69621, Villeurbanne (France)*

Abstract

Deep drawing complex composite parts including strong geometrical non-linearities are currently of major interest. Such forming process induces non-monotonous variations in bending and in-plane shear deformation modes. Moreover, it is experimentally shown that these specific variations lead to an hysteretic behavior of the material. Hence, non dissipative models are no longer appropriate to accurately describe the behaviour since these variations of load cannot longer be neglected. The objective of this paper is therefore to propose an anisotropic model under large strains capable of describing the hysteretic trajectories of the material's behavior. For this purpose, a fractional derivative approach was applied and identified. Through this hysteretic approach, it is now possible to predict the shape, shear and bending strain more accurately when the fabric undergoes heavy transformation. This model also gives the possibility to predict the residual stress and plastic strain. These predictions lead to quantify the spring back of the material when the punches are removed, which is very important since new deep drawing strategies are emerging. Discretization procedures for fractional derivatives models are described and Matlab source codes are also provided.

Keywords: Woven fabric, Hysteresis, Fractional derivatives, Large strains, Anisotropy

1. Introduction

Even though composite materials forming is still subject to many lines of research, industrial issues are also constantly evolving. Since the shapes of the parts used in automotive, aeronautics or even aerospace industry are more and more complex, it is important to propose richer models and closer to the physical reality of the material behavior. One commonly used composite forming process is Resin Transfer Molding (RTM) [1–3]. This process consists in forming a dry fabric and then injecting liquid state resin. In order to simulate the first step of this process, models already exist at different scales. Models at the microscopic scale (fiber scale) [4, 5] or at the mesoscopic scale (yarn scale) [6–9] allow to have local information. However, the objective of this article is to get the stress field of the final part as well as the defects induced by the

*Corresponding author
Email address: nahiene.hamila@insa-lyon.fr (Nahiene Hamila)

forming process at the macroscopic scale (wrinkles, shear angle, residual stresses, ...). In addition, the strong geometric nonlinearities induced by the shape of the molds induce phenomena that were not necessarily of major importance a few years ago. Moreover, new stamping methods begin to be investigated such as incremental forming [10–14]. Indeed, cyclic loading in bending and shear can appear. The models usually used for numerical simulation such as hyperelastic type (or reversible) [15–20] are not enough sophisticated to take into account these phenomena. To answer this issue, models have already been proposed dealing with viscoelasticity under finite strains [21–25] or visco-elastoplasticity under small strains [26]. However, it is important to notice the strong geometrical nonlinearities due to the complex shapes of the mold and punches. Hence, the fabric undergoes huge transformations. Thus, small strains assumptions are no longer valid and the set of hypotheses induced are de facto also unsuitable. Consequently, the previous models are not compatible anymore with the behavior of a dry fabric (the viscoelastic models are not adapted, the hyperelastic models either). A first approach, using a sophisticated nested surfaces, has already been proposed recently in [27]. However, this model is difficult to integrate into a finite element calculation software. Indeed, given the large amount of parameters, the identification procedure can be difficult and the evolution of the hysteresis loops is approximated by using nested yield surfaces theory (see [27]). It is therefore important to establish a new irreversible model to describe the dissipative mechanism with a hysteretic constitutive law. The behavior of the material during cyclic loading is still in the field of research since only few works have already been published. Experimental approaches are up-to-date and are of serious interest for the automotive industries through incremental forming methods. The incremental draping process generally induces shear and bending loading variations [28–30]. Recent works have also begun to emerge to characterize composite parts once the draping is done [31]. The history of the material must be taken into account making the hyperelastic models commonly used for dry fabrics unsuitable. Finally, the objective of this work is to propose a model with few parameters to describe the behavior of a composite material subjected to cyclic loading under large strains. Experimentally, the behavior of the material when subjected to cyclic loading is strongly nonlinear [22, 30, 32–35]. Indeed, the behavior during a load cycle leads to a hysteretic loop. To fit this specific behavior, a fractional derivative approach is adopted. Many studies have shown the interest of this approach [36–39]. Indeed, fractional derivatives can be used for different topics such as fatigue limits of polymers and elastomers in the frequency domain [40, 41], time-dependent models for thermoplastics or viscoelastic models under small strains [26, 42–44] and other applications in the field of polymers [45–50]. The objective of this article is to adapt this method and apply it to model the anisotropic behavior of a fabric under large strain. In addition, the fractional derivative is a tool that has already been used several times in mechanical and numerical simulation problems [51, 52]. Its use in various fields makes this tool a major asset in the development of the model and its integration into a finite element code. Moreover, when draping a composite material, several deformation modes occur. For thin fabrics, bending and in-plane shearing are assumed to be the main dissipative modes. Different

strain modes may be linked and couplings between elongation and shear [35, 53] or between elongation and bending [53, 54] or even between bending and shearing [32, 55] could be introduced. The deformation of a woven fabric is mainly due to the relative movement between the fibers. These fibers are supposed quasi-inextensible and it is assumed here that the stretching does not dissipate energy. The tension/compression behavior is thus supposed to be elastic. As a result, only out of plane bending and in-plane shear will be characterized here to model the cyclic loading behavior. In addition, numerous works propose numerical approaches to integrate fractional derivative models in finite element softwares [26, 51]. This work presents a new way of integrating fractional derivative computing without the need for numerical approximation since the theoretical calculation and thus the exact formulation can be done upstream. This will be presented in parts. In the first part a small introduction to fractional derivatives is presented. The second part will describe the mechanical model for shearing and bending, and in the third part identification of the parameters will be explained followed by some results and discussions.

2. Introduction to fractional derivative

Modelling cyclic loading can be done in different manners. It is possible to develop complex and sophisticated models with many parameters. The difficulty of the identification procedures is then directly proportional to the number of parameters needed for these models. Otherwise, there are specific methods to describe hysteresis more directly. In this case, it is mandatory to perform a coupling between a dissipative model and a model that describes hysteretic loops. Several methods describe these specific loops based on nested surfaces of Mroz [56], completed by Prager [57] and then Ziegler [58] or adapted by the recent work of Denis et al. [27]. This model, however, requires many parameters and is difficult to identify. Other works using the fractional derivative method have been done and proven effective [26, 51, 52]. In [26], time dependent and viscoelastic models have been written under small strains and they do not require many parameters. This approach allows having an accurate numerical description of a physical phenomenon while remaining easy to identify. This means that it is possible to extend this work to apply the fractional derivative method under anisotropic large strains.

Moreover, there are several ways to calculate a fractional derivative. Depending on the case, some methods are more suited than others. For example, the fractional derivative of Weyl [59] is defined for periodic functions. In order to be integrated into a finite element software, the discretization based on the fractional derivative of Grunwald-Letnikov [39, 52] may be used. Indeed, it has the advantage of not involving integral approximation such as Simpson, Gauss or other, but only a sum calculation. However, the calculus of this sum cannot be infinite and induces small but inevitable errors. Finally, in the work presented here, it is shown that it is possible to use the fractional derivative of Caputo [49, 60]. Further details on the calculation are presented below. Since details on the calculation of fractional derivatives are already presented in many

works [36, 38, 39], only few preliminary definitions are given in the next section.

2.1. Preliminary calculations for fractional derivatives

In this part, few preliminary calculations for fractional derivatives are described. Indeed, they are useful for the development of the model in section 3.

2.1.1. Definition of the fractional derivative

The use of the fractional derivative allows to establish a model with few parameters and to describe complex phenomena such as hysteretic loops. In general, the fractional derivative consists in calculating the derivative of a function but for a non-integer order. Usually, the order of the derivative can vary between the order 0 (return as result the function itself) and the order 1 (the result is the usual derivative of the function (Fig. 1)). The parameter that controls the order of the derivative is denoted α in Eq. (1). This parameter may evolve during transformations. Additional parameters may change the response of the fractional derivative by making it undergo translations (homotheties) and inclinations. All of these parameters are presented in this section.

In addition, there are several definitions of the fractional derivative, each having their own specificities. The Rieamann-Liouville approach is one of the first fractional derivative definitions and it is a purely mathematical approach [37, 39, 61]. Podlubny describes this approach as not optimal for mechanical problems with particular initial conditions (§2.4.1, page 78, in Podlubny's book [36]). This is why the definition of the fractional derivative of Caputo is more interesting. Caputo proposed a new definition of the fractional derivative based on a physical approach. His definition is often used in the field of mechanics for viscous problems or even plasticity problems involving the history of the material. Furthermore, it is possible to analytically calculate the fractional derivative of a linear function. It is shown in Section 3.2 that only the Caputo derivative of a linear and a constant function are needed to describe the hysteretic behavior. As a result, the next part of this article will detail the calculus for a linear function.

2.1.2. Definition of the Caputo's fractional derivative and its properties

As previously stated, Caputo's fractional derivative is the most suitable for solving mechanical problems. It is thus important to describe this derivative in the general case as well as its properties. Secondly, the demonstration of the derivative of a power function in the sense of Caputo is presented since it is not trivial. The first important definition is therefore the fractional derivative in the sense of Caputo for any function $f(t)$ defined and differentiable over an interval $[a, b]$ (Eq. (1)).

$$D_a^\alpha f(x)\Big|_c = \frac{1}{\Gamma(n-\alpha)} \int_a^x \frac{f^{(n)}(t)}{(x-t)^{\alpha+1-n}} dt, \quad n \in \mathbb{N} \tag{1}$$

In Eq. (1) appear important quantities as listed below:

- The Gamma function at the denominator of the first term. This particular function is defined through Eq. (2) and one of its major intrinsic properties by Eq. (3).

$$\Gamma(z) = \int_0^{+\infty} e^{-x} x^{z-1} dx, \quad z \in \mathbb{R}_*^+ \tag{2}$$

This equation has some properties that may be useful for the calculation as the recurrence relation presented in Eq. (3).

$$\Gamma(z+1) = z\Gamma(z) \tag{3}$$

The relationship between a factorial quantity and the Gamma function is presented in Eq. (4).

$$\Gamma(z+1) = z! \tag{4}$$

- The function subjected to the fractional derivative, noted $f(t)$ and its full order derivatives $f^{(n)}(t)$.
- Parameter α represents the order of the derivative such as $\alpha \in]0,\ 1[$.
- Parameter n associated to the definition of the fractional derivative and represents the derivation order of the function $f(t)$.
- Parameter a corresponds to the lower integration boundary of the function, if the function is set to an interval $[a, b]$.

The most general power function may be defined by Eq. (5):

$$f(x) = b(x-a)^{\lambda} + d, \quad \lambda \in \mathbb{Z},\ b \in \mathbb{R},\ d \in \mathbb{R},\ a \in \mathbb{R} \tag{5}$$

Since the fractional derivative is distributive and multiplicative [36, 49], the derivative of Eq. (5) can be split into two independent terms. A first term corresponding to the power function and a second term corresponding to a constant:

$$D_a^{\alpha} f(x)\Big|_c = D_a^{\alpha}\left(b(x-a)^{\lambda} + d\right)\Big|_c = bD_a^{\alpha}\ (x-a)^{\lambda}\Big|_c + D_a^{\alpha}\ d\Big|_c = bD_a^{\alpha}\ (x-a)^{\lambda}\Big|_c \tag{6}$$

The fractional derivative of a constant from Caputo point of view is, by definition, equal to zero.
A last property of the fractional derivative is the Beta function that links the Gamma function to an integral calculation.

$$\beta(z, w) = \int_0^1 x^{z-1}(1-x)^{w-1} dx, \quad z \in \mathbb{R}_*^+, w \in \mathbb{R}_*^+ \tag{7}$$

This beta function can also be written as below:

$$\beta(z, w) = \frac{\Gamma(z)\Gamma(w)}{\Gamma(z+w)} \tag{8}$$

Since the major properties and the general Caputo's definition are described, it is possible to exploit them through a concrete example that suits to the models presented in the next section (section 3).

2.1.3. *Fractional derivative of a power function*

In section 3, it is shown that the function to derive is a simple linear function. Considering the general case as defined in Eq. (9), it is then possible to deduce its fractional derivative.

$$f(x) = (x-a)^{\lambda}, \quad \lambda \in \mathbb{Z},\ a \in \mathbb{R} \tag{9}$$

The fractional derivative of Eq. (9) can be computed rigorously by a variable change and by the use of the functions and properties defined above. The fractional derivative is written as presented in Eq. (10).

$$D_a^{\alpha} f(x)\Big|_c = \frac{d_a^{\alpha}(x-a)^{\lambda}}{d(x-a)^{\alpha}}\Big|_c = \frac{1}{\Gamma(n-\alpha)} \int_a^x \frac{((t-a)^{\lambda})^{(n)}}{(x-t)^{\alpha+1-n}} dt \tag{10}$$

Calculation details are presented below:

- Starting by calculating the n-th times derived function, it comes:

$$((t-a)^{\lambda})^{(n)} = \frac{\lambda!}{(\lambda-n)!}(t-a)^{\lambda-n}, \quad such\ as\ \lambda\ \geq\ n \tag{11}$$

- By using this result, Eq. (10) becomes:

$$D_a^{\alpha}(x-a)^{\lambda}\Big|_c = \frac{1}{\Gamma(n-\alpha)} \frac{\lambda!}{(\lambda-n)!} \int_a^x \frac{(t-a)^{\lambda-n}}{(x-t)^{\alpha+1-n}} dt \tag{12}$$

- By applying the variable change, it allows to set the integration boundaries between $[0,1]$. It is then possible to use the Beta function to simplify the integral:

$$t = a + s(x-a) \rightarrow \begin{cases} t = a \Rightarrow s = 0 \\ t = x \Rightarrow s = 1 \\ dt = (x-a)ds \end{cases} \tag{13}$$

This leads to the following formulation:

$$D_a^{\alpha}(x-a)^{\lambda}\Big|_c = \frac{(x-a)^{\lambda-\alpha}}{\Gamma(n-\alpha)} \frac{\lambda!}{(\lambda-n)!} \int_0^1 \frac{s^{\lambda-n}}{(1-s)^{1-n+\alpha}} ds \tag{14}$$

- Using the Beta function, it simplifies Eq. (14):

$$\beta(z,w) = \int_0^1 x^{z-1}(1-x)^{w-1} dx \rightarrow \begin{cases} x = s \\ z = \lambda - n + 1 \\ w = n - \alpha \end{cases} \tag{15}$$

leading to the following Beta function:

$$\beta(\lambda - n + 1, n - \alpha) = \frac{\Gamma(\lambda - n + 1)\Gamma(n-\alpha)}{\Gamma(\lambda + 1 - \alpha)} \tag{16}$$

- Using the property from Eq. (4), it comes:

$$\Gamma(z+1) = z! \rightarrow \begin{cases} \lambda! = \Gamma(\lambda+1) \\ (\lambda-n)! = \Gamma(\lambda-n+1) \end{cases} \tag{17}$$

- By considering Eq. (17) into Eq. (14), it comes Eq. (18).

$$D_a^\alpha (x-a)^\lambda \Big|_c = \frac{\Gamma(n-\alpha)\Gamma(\lambda+1)\Gamma(\lambda-n+1)}{\Gamma(n-\alpha)\Gamma(\lambda-n+1)\Gamma(\lambda+1-\alpha)}(x-a)^{\lambda-\alpha} \tag{18}$$

Finally, the fractional derivative result of Eq. (5) is Eq. (19).

$$D_a^\alpha (x-a)^\lambda \Big|_c = \frac{\Gamma(\lambda+1)}{\Gamma(\lambda+1-\alpha)}(x-a)^{\lambda-\alpha} \tag{19}$$

Section 3 of this article needs the fractional derivative of a linear function defined by Eq. (20).

$$f(x) = x - x_0 \tag{20}$$

It is the same type of Eq. (9) but considering $\lambda = 1$ and $a = x_0$ so its derived form is described by Eq. (21).

$$D^\alpha (x-x_0) \Big|_c = \frac{\Gamma(2)}{\Gamma(2-\alpha)}(x-x_0)^{1-\alpha} \tag{21}$$

The description of this function by arbitrarily imposing $x_0 = 1$ and by varying the variable α is presented in Fig. 1. However, it is important to take into account the validity domain of this function. Indeed, since the power is of the order $1-\alpha$ and $\alpha \in [0,1]$ then it is imperative that $x \geq x_0$. It is therefore important to separate the cases:

$$D^\alpha (x-x_0) \Big|_c = \begin{cases} \frac{\Gamma(2)}{\Gamma(2-\alpha)}(x-x_0)^{1-\alpha} & if\ x \geq x_0 \\ -\frac{\Gamma(2)}{\Gamma(2-\alpha)}(x_0-x)^{1-\alpha} & if\ x < x_0 \end{cases} \tag{22}$$

Since the function is linear and odd:

$$f(x_0 - x) = -f(x - x_0) \tag{23}$$

Through this property it is possible to generalize Eq. (22) to be valid whatever the validity domain of this function (for this particular case only):

$$D^\alpha (x-x_0) \Big|_c = \text{sign}(x-x_0) \cdot \frac{\Gamma(2)}{\Gamma(2-\alpha)} \cdot |x-x_0|^{1-\alpha} \tag{24}$$

Moreover, it is possible to control the behavior of the fractional derivative accurately with very few parameters. This advantage makes this method simple and effective even though the model development is not trivial. In Fig. 1, different configurations of the fractional derivative of the function defined Eq. (20) are

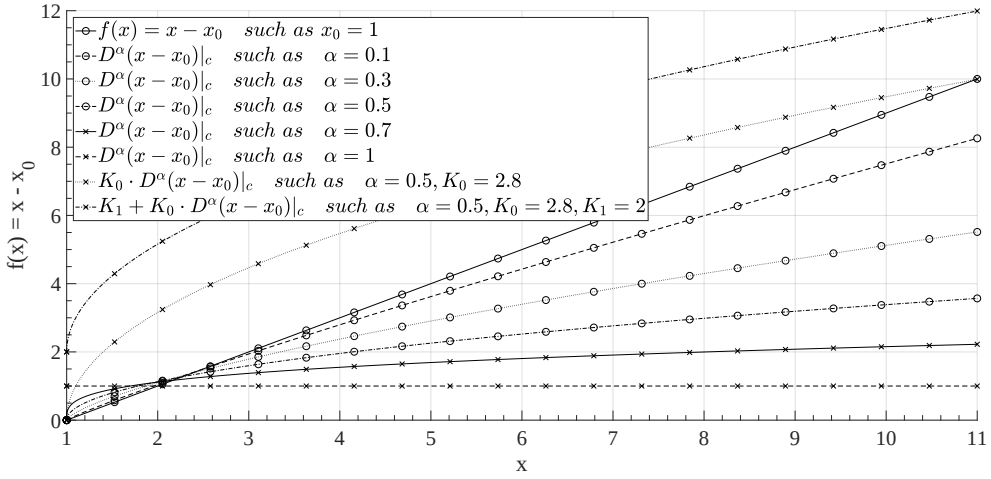

Fig. 1: Fractional derivatives of the function $f(x) = x - 1$ under variation of α.

plotted (5 configurations by increasing the derivative order and two other configurations corresponding to the homothety and orientation of the result). Indeed, by posing the function $\tilde{f}(x)$ defined by Eq. (25), and by varying its parameters it is possible to rotate and/or translate the fractional derivative.

$$\tilde{f}(x) = K_1 + K_0 \cdot D^\alpha (x - x_0)^\lambda \Big|_c, \quad K_0 \in \mathbb{R} \; and \; K_1 \in \mathbb{R} \tag{25}$$

Finally, it is also possible to vary the parameters K_1, K_0 and α according to the abscissa. Eq. (25) may finally be rewritten as defined by Eq. (26)

$$\tilde{f}(x) = K_1(x_0) + K_0(x_0) \cdot D^{\alpha(x_0)} (x - x_0)^\lambda \Big|_c \tag{26}$$

Functions $K_1(x_0)$, $K_0(x_0)$ or $\alpha(x_0)$ can be defined either by constants, linear functions or even polynomials. All applied descriptions are defined in section 3

Fractional derivatives may be used without doing any numerical approximations since the integration calculation could be formally done. This is remarkable since it reduces both the calculation time and errors accumulated each time step. The goal is now to apply this method to describe the in-plane shear and bending hysteretical behavior of a thin composite reinforcement.

3. Finite strain anisotropic models for cyclic loading

The objective of this section is to adapt the fractional derivative method to describe the hysteretic loops of the material for cyclic loading in shear and bending. At first, an experimental approach is made. Moreover, it is important to distinguish the dissipative and the hysterical behavior. The dissipative behavior describes the lower and upper boundaries of the experimental data (Fig. 5). The hysteretical behavior only concerns the hysteretic loops also shown in Fig. 5 or Fig. 3.

Regarding the in-plane shear behavior, the dissipative part is already well described by the model proposed by Denis et al. [27]. Concerning the bending loading, it is only described by an empirical approach.

Remark 0. In this article, second order tensors are written using bold letters (**S**,**E**,**F**...), vectors (first order tensors) with an over bar ($\overline{u}$, $\overline{v}$, ...) and the scalar quantities by normal font.

Remark 1. Several hypotheses were taken into account for the dissipative calculation such as:

- Since the yarns are considered almost inextensible, the behavior in tension/compression is supposed elastic. Only out of plane bending and in-plane shearing modes dissipate energy.
- The dissipation modes are decoupled, i.e. the in-plane shear has no influence on the bending and vice versa.
- As the yarns do not elongate, the kinematics of the in-plane shear dissipation necessarily follows a kinematics of pure shear. The associated formulation is defined in Eq. (31).

3.1. Experimental approach under cyclic loading

In this part, an Hexcel® G1151 dry fabric composite material composed by carbon fiber is used. The cyclic shear test follows the Picture Frame Test procedure (Fig. 2). Since this test imposes a homogeneous pure shear field on the whole specimen, it is usually used to characterize the fabric. The bending test is a simple test that gets the evolution of the bending moment as a function of the curvature. For this article, the experimental data for bending behavior is taken from De Bilbao et al. [33]. The hysteresis path is assumed to follow the Kawabata theory [62].

3.1.1. Picture Frame Test

The Picture Frame test consists of placing a sample of dry fabric in an articulated frame (Fig. 2) [22, 63, 64]. Experimental results are presented in Fig. 2 from four specimens.

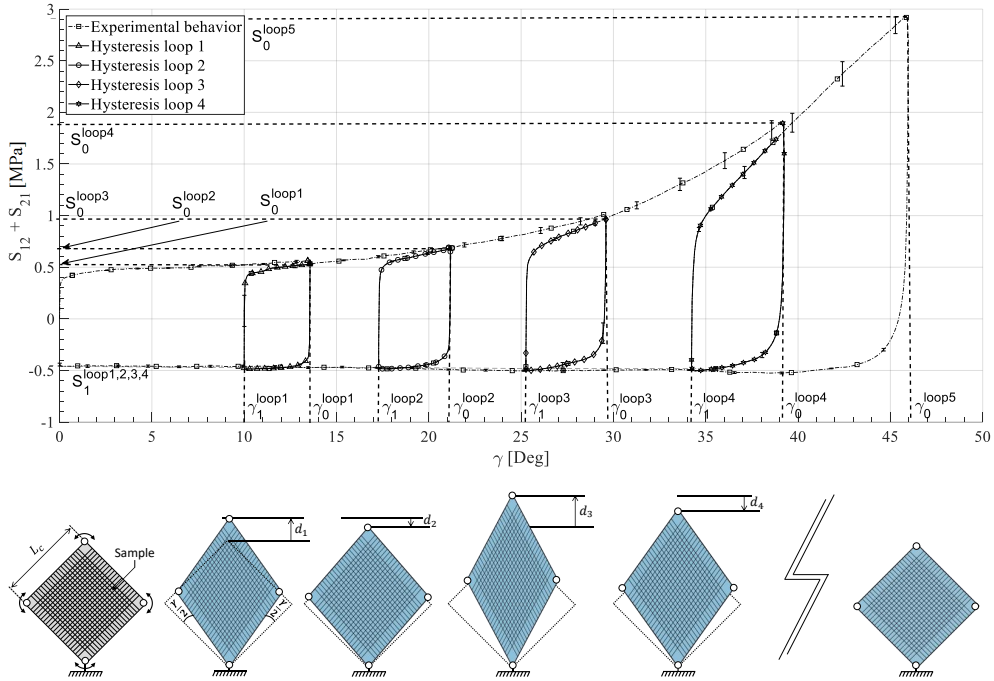

Fig. 2: Hexcel® G1151 behavior under cyclic loading on a Picture Frame Test.

In this type of experiment, the imposed load is the displacement of the movable jaw: d_1, d_2 and d_3 in Fig. 2. The relation shear angle-displacement is thus defined by Eq. (27) (where L_c represents the length of one side of the frame, here $L_c = 180 \cdot \sqrt{2}$).

$$\gamma(d) = \frac{\pi}{2} - 2\text{acos}\left(\frac{\sqrt{2}}{2} + \frac{d}{2 \cdot L_c}\right) \tag{27}$$

In addition, it is easily possible to notice the hysteretical behavior of the material once subjected to cyclic loading.

3.1.2. Simple Bending Test

As it was said before, the experimental behavior for the out of plane bending mode (Fig. 3) is taken from the work of De Bilbao et al. [33] which describes the evolution of the bending moment as a function of the curvature. Since no cyclical loading has already been applied for the bending experiment on composite woven fabrics, the behavior is supposed to follow an hysteretical path. This specific path can be associated to the behavior which is possible to get through a Kawabata experiment. The authors of this article being not able to reach a Kawabata experimental set-up, the behavior was firstly supposed. After comparison with a deep-drawing experiment (see Fig. 19), it is shown that the results satisfied the assumption. However, further experiments still need to be done. This cyclical behavior corresponding to a Kawabata experiment is shown by the picture inserted in Fig. 3. Moreover, for the identification, it is assumed that the shape of

the return path (from a maximum moment to zero) is following the shape proposed in [65]. On Fig. 2 and Fig. 3, the loads presented are positive for clarity reasons. However, the models work for either positive or negative loading.

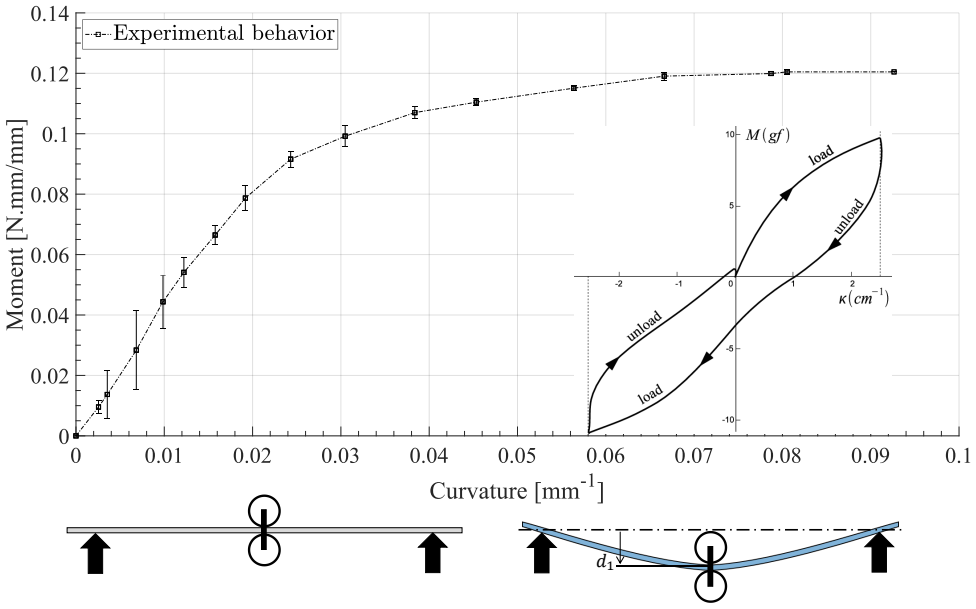

Fig. 3: Bending test on Hexcel® G1151 dry fabric and Kawabata approach for cyclic loading [33, 62].

3.2. Constitutive law for in-plane shear deformation mode

The work of Denis et al. [27] proposes a type of law from a thermodynamical approach. This law is applied in this paper. Some details are defined below.

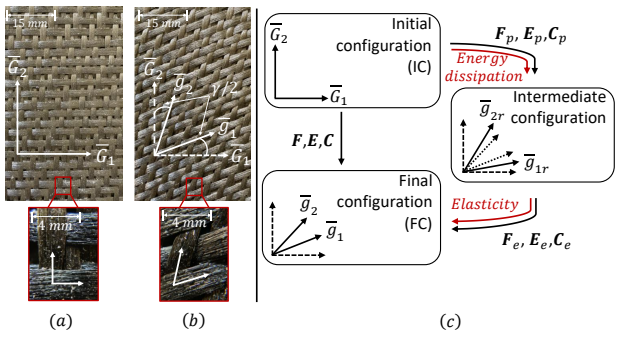

Fig. 4: Intermediate configuration theory: Initial (a) and actual (b) basis of the woven fabric. Theory illustration (c) with description of the tensors.

Using the description of intermediate configuration as shown in Fig. 4(c), the additive decomposition of

Green-Naghdi adapted for anisotropic materials under large strains is used in Eq. (28).

$$\mathbf{E}_e = \mathbf{E} - \mathbf{E}_p \tag{28}$$

Usually associated with the previous decomposition, the multiplicative decomposition of Kröner-Lee [66, 67] is defined below:

$$\mathbf{F} = \mathbf{F}_e \cdot \mathbf{F}_p \tag{29}$$

In Eqs. (28) and (29) appear different quantities as defined below:

- $\mathbf{E}$ is the total Green-Lagrange tensor
- $\mathbf{E}_e$ is the elastic contribution of the Green-Lagrange tensor
- $\mathbf{E}_p$ is the dissipative contribution of the Green-Lagrange tensor
- $\mathbf{F}$ is the transformation gradient imposed by the user or the simulation. This is the load applied during a simulation (see Eq. (30)).
- $\mathbf{F}_e$ is the elastic contribution of the transformation gradient
- $\mathbf{F}_p$ is the dissipative contribution of the transformation gradient. The hypothesis of non-elongation of the fibers thus imposes a kinematics of pure shear for this dissipation (see Eq. (31)).

Given the assumptions mentioned previously and the two decompositions (Eqs. (28) and (29)) described above, it is possible to define the tensors in a general manner.

$$\mathbf{F} = \sum_i \sum_j F_{ij} \cdot \left(\overline{G}_i \otimes \overline{G}_j\right) = \sum_i \overline{g}_i \otimes \overline{G}^i, \qquad j = 1, 2, \qquad i = 1, 2 \tag{30}$$

With $\overline{G}_1$ and $\overline{G}_2$ the direction of the fibers at the initial state as shown in Fig. 4(a), and $\overline{G}^1$ and $\overline{G}^2$ the countravariant basis.

$$\mathbf{F}_p = \cos\left(\tfrac{\gamma_p}{2}\right)\left(\overline{G}_1 \otimes \overline{G}_1 + \overline{G}_2 \otimes \overline{G}_2\right) + \sin\left(\tfrac{\gamma_p}{2}\right)\left(\overline{G}_1 \otimes \overline{G}_2 + \overline{G}_2 \otimes \overline{G}_1\right) \tag{31}$$

The dissipative contribution is defined above (Eq. (31)),where γ_p is the shear angle from the dissipative contribution. It is calculated in such a way that the defined yield function Eq. (34) tends to zero. It therefore contributes to the plastic flow following the maximal dissipation theory. Considering the Kröner-Lee multiplicative decomposition, it is possible to deduce the elastic component of the transformation gradient.

$$\mathbf{F}_e = \mathbf{F} \cdot \mathbf{F}_p^{-1} \tag{32}$$

Following the additive decomposition of Green-Naghdi it is possible to define the elastic contribution of the deformation:

$$\mathbf{E}_e = \frac{1}{2}\left(\mathbf{F}_p^t \cdot \left(\mathbf{F}_e^t \cdot \mathbf{F}_e - \mathbf{I}_d\right) \cdot \mathbf{F}_p\right) \tag{33}$$

$\mathbf{I}_d$ being the identity tensor. From the definitions described above, it is possible to establish the dissipative law using the maximum dissipation principle [68–70]. Details are present in the work of Denis et al. [27]. This specific dissipative law describes a yield surface that evolves as a function of the shear angle. In order to minimize the energy, a Newton-Raphson algorithm is used to determine the dissipative contribution of this deformation noted γ_p so that the yield function tends to zero.

$$f_s\left(\gamma_p\right) = \left|\mu K_{sh}\left(F_{11}F_{21} + F_{12}F_{22} - \sin\left(\gamma_p\right)\right) - \sum_{i=1}^{4} Q_i \gamma_p^i\right| - \left(S_y + \sum_{i=1}^{4} A_i \left|\gamma_p\right|^i\right) \tag{34}$$

With:

- K_{sh} the shear stiffness of the fabric
- Q_i the polynomial parameters representing kinematic hardening
- A_i the polynomial parameters representing isotropic hardening
- S_y corresponds to the yield stress
- μ the surface density of the material
- F_{11}, F_{12}, F_{21} and F_{22} the components $1-1, 1-2, 2-1$ and $2-2$ of the transformation gradient

Dissipative behavior is only present if the yield function is positive. If the yield function is negative, the behavior is either elastic or hysteretic.

Once the parameter γ_p is determined, it is then possible to update the elastic contribution of the Green-Lagrange tensor (by the additive decomposition of Green-Naghdi adapted for large deformations, Eq. (28)) and finally to determine the value of the Second Piola-Kirchhoff stress tensor, noted $\mathbf{S}$.

To define this tensor, it is possible to describe the evolution of the stress as being linearly connected to the elastic deformation tensor of Green-Lagrange $\mathbf{E}_e$.

$$\begin{aligned}\mathbf{S} = \mu\big[&K_1\left(\mathbf{E}_e : \left(\overline{G}_1 \otimes \overline{G}_1\right)\right) \cdot \left(\overline{G}_1 \otimes \overline{G}_1\right) + K_2\left(\mathbf{E}_e : \left(\overline{G}_2 \otimes \overline{G}_2\right)\right) \cdot \left(\overline{G}_2 \otimes \overline{G}_2\right) + \\ &K_{sh}\left(\mathbf{E}_e : \left(\overline{G}_1 \otimes \overline{G}_2 + \overline{G}_2 \otimes \overline{G}_1\right)\right) \cdot \left(\overline{G}_1 \otimes \overline{G}_2 + \overline{G}_2 \otimes \overline{G}_1\right)\big]\end{aligned} \tag{35}$$

Where:

- K_1, K_2 are material coefficients describing the stiffness in the warp and weft direction respectively

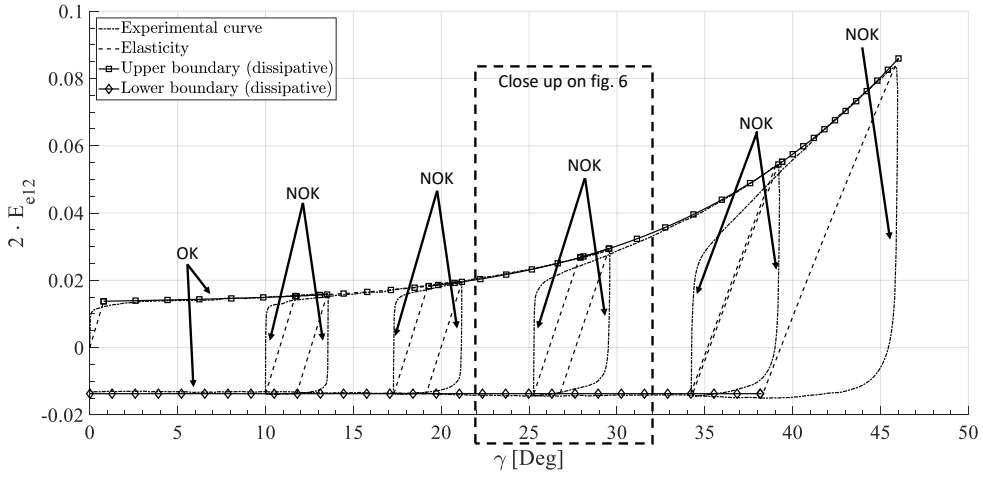

Fig. 5: Result after application of the dissipative model without taking into account the fractional derivatives method to model hysteretic loops.

By imposing a pure shear load (to be in the same context as the experiment) by Eq. (36), and using the identified parameters (Table 2), Eq. (35) allows to model the upper and lower asympotes of the experimental curve (Fig. 5).

$$\mathbf{F} = \cos\left(\frac{\gamma}{2}\right)\left(\overline{G}_1 \otimes \overline{G}_1 + \overline{G}_2 \otimes \overline{G}_2\right) + \sin\left(\frac{\gamma}{2}\right)\left(\overline{G}_1 \otimes \overline{G}_2 + \overline{G}_2 \otimes \overline{G}_1\right) \tag{36}$$

This model makes possible to have a very fair description of the loading phases but does not contribute in any case to the hysteretic loops. The objective is therefore to transform the elastic evolution (AB and DC paths in Fig. 6) into hysteretic ways. Fig. 6 shows the current state of the deformation and the purpose of the next paragraph. The idea is to implement the fractional derivative and adapt it to model the hysteretic loops.

As it can also be seen, only the diagonal components of the Piola-Kirchhoff II tensor represent the shear behavior of the fabric. Thus, the fractional derivative is only effective on these components. For clarity, and since the strain and stress tensors are symmetric, only the Piola-Kirchhoff II component S_{12} is presented here. It is exactly the same protocol for the component S_{21}. However, on every figure, the sum of the components $S_{12} + S_{21}$ is displayed.

$$\mathbf{S} : \left(\overline{G}_1 \otimes \overline{G}_2\right) = S_{12} = K_{sh}\left(\mathbf{E}_e : \left(\overline{G}_1 \otimes \overline{G}_2\right)\right) = K_{sh} E_{e12} \tag{37}$$

In addition, during an unloading phase, the dissipative variable γ_p is constant. It is thus possible to define the stress $\mathbf{S}$ as being only dependent on the variable γ. During the unloading, the evolution of the stress, using the fractional derivative method can be described as defined by Eq. (38).

$$S_{12} = \frac{1}{2} \cdot S_j^{loopi} + \mu \cdot K_{sh} \cdot B \cdot \left.\frac{d^\alpha E_{e12}}{d\gamma^\alpha}\right|_c \tag{38}$$

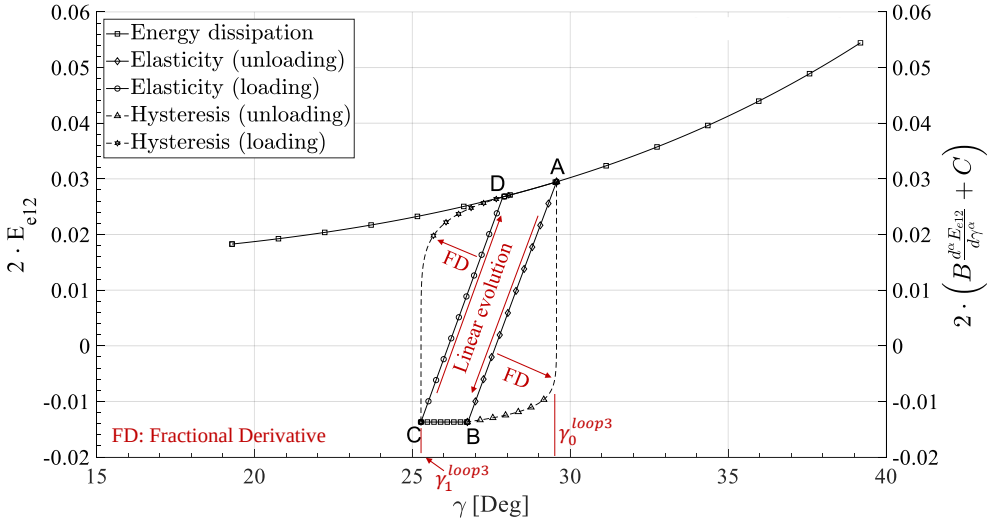

Fig. 6: Objective of the fractional derivative application: transform linear evolution into hysteretic loop. Energy dissipation and elasticity referred to the left axis. Hysteretic behavior referred to the right axis.

Where:

- S_j^{loopi} is the value of the stress when unloading starts or reloading starts (see Fig. 2).
- B is a parameter allowing the orientation of the fractional derivative. This parameter is constant within a loop but may vary according to the active loop (see section 2).
- j corresponds to the case at the time t. If it is the unloading phase of the hysteretic loop then $j = 0$, if it is the ascending phase (reloading) of the hysteretic loop then $j = 1$ (see Fig. 2).

According to Eq. (28) it is possible to define the quantity to derive from the elastic strain tensor:

$$E_{e12} = E_{12} - E_{p12} = \frac{1}{2} \cdot \left(\mathbf{F}^t \mathbf{F} - \mathbf{I}_d \right) - \frac{1}{2} \cdot \left(\mathbf{F}_p^t \mathbf{F}_p - \mathbf{I}_d \right) = \frac{1}{2} \cdot \left((F_{11} F_{12} + F_{21} F_{22}) - \sin(\gamma_p) \right) \tag{39}$$

By using usual anisotropic invariants, it is possible to define a link between Eq. (38) and the total shear angle imposed by the load. These invariants are defined by Eq. (40). It is important to note that the fibers of the materials are assumed inextensible. This assumption implies that the invariants I_{41} and I_{42} tend to 1:

$$Anisotropic\ invariants \rightarrow \begin{cases} I_{41} = \overline{G}_1 \cdot \mathbf{C} \cdot \overline{G}_1 \approx 1 & \forall \mathbf{F} \\ I_{42} = \overline{G}_2 \cdot \mathbf{C} \cdot \overline{G}_2 \approx 1 & \forall \mathbf{F} \\ I_{421} = \overline{G}_2 \cdot \mathbf{C} \cdot \overline{G}_1 \\ I_{cp} = \sin(\gamma) = \frac{I_{421}}{\sqrt{I_{41} * I_{42}}} \end{cases} \tag{40}$$

With $\mathbf{C} = \mathbf{F}^t\mathbf{F}$.

From these invariants it is possible to define the shear angle γ.

$$\sin(\gamma) = \frac{I_{421}}{\sqrt{I_{41} * I_{42}}} \approx I_{421} = F_{11}F_{12} + F_{21}F_{22} \tag{41}$$

Using this definition and the one from Eq. (33) it is possible to define the relation between the elastic deformation and the shear angle γ .

$$E_{e12} = \frac{1}{2} \cdot (\sin(\gamma) - \sin(\gamma_p)) \tag{42}$$

Considering Fig. 2, the fractional derivative starts from the beginning of the unloading, i.e. from $\gamma = \gamma_0^{loopi}$. Moreover, given the angle variation $(\gamma - \gamma_0^{loopi})$, it is experimentally observable that $\gamma - \gamma_0^{loopi}$ varies within a range of $[0, 10]$ degrees (5° in the case of Hexcel® G1151, Fig. 6). Therefore, it is possible to approximate the sinus at its first order (such as $sin(\gamma) \approx \gamma$). It is the same for the reload phase in the hysteresis loop. In this case, the angle variation is $\gamma - \gamma_1^{loopi}$ in Fig. 2. In order to generalize the model as much as possible, the index j corresponds to the studied case. If it is an unloading phase then $j = 0$, if it is a reload phase (still in the hysteresis loop) then $j = 1$.

$$\begin{cases} \sin\left(\gamma - \gamma_j^{loopi}\right) \approx \gamma - \gamma_j^{loopi} \\ E_{e12} = \frac{1}{2} \cdot \left(\left(\gamma - \gamma_j^{loopi}\right) - \sin(\gamma_p)\right) \end{cases} \tag{43}$$

By updating Eq. (38) it comes:

$$S_{12} = \frac{1}{2} S_j^{loopi} + \mu \cdot K_{sh} \cdot B \cdot \left. \frac{d^\alpha \left(\frac{1}{2} \cdot \left(\left(\gamma - \gamma_j^{loopi}\right) - \sin(\gamma_p)\right)\right)}{d\gamma^\alpha} \right|_c \tag{44}$$

In addition, given the properties previously established for the Caputo fractional derivative and since γ_p is constant, Eq. (44) can be written as presented by Eq. (45).

$$\left. \frac{d^\alpha \left(\frac{1}{2} \cdot \left(\left(\gamma - \gamma_j^{loopi}\right) - \sin(\gamma_p)\right)\right)}{d\gamma^\alpha} \right|_c = \frac{1}{2} \cdot \text{sign}\left(\gamma - \gamma_j^{loopi}\right) \cdot \frac{\Gamma(2)}{\Gamma(2-\alpha)} \cdot \left|\left(\gamma - \gamma_j^{loopi}\right)\right|^{1-\alpha} \tag{45}$$

Finally, the evolution of the stress can be written as follows:

$$S_{12} = \frac{1}{2} S_j^{loopi} + \mu \cdot K_{sh} \cdot B_{sh} \cdot \text{sign}\left(\gamma - \gamma_j^{loopi}\right) \cdot \frac{\Gamma(2)}{\Gamma(2-\alpha)} \cdot \left|\gamma - \gamma_j^{loopi}\right|^{1-\alpha} \tag{46}$$

With:

$$B_{sh} = \frac{1}{2} \cdot B \tag{47}$$

Section 4 shows different cases of use of this model, the number of parameters to identify as well as the advantages and disadvantages of each model are also presented.

3.3. Empirical law for bending mode

The objective is to define a model to describe the bending behavior of the material. The approach in this subsection is purely empirical and shows that the fractional derivative can also be used for direct approaches. The dissipative phase is described from an exponential function to match the bending moment as a function of the curvature Eq. (48). The hysteretic loops are also defined from a fractional derivative approach. Moreover, it is possible to see by comparing Figs. 2 and 3 that the behavior is very different.

$$M = M_{max} \cdot \left(1 - \exp\left(-\frac{C}{K}\right)\right) \tag{48}$$

Where:

- M_{max} is the maximum amplitude of the bending moment (see Fig. 3).
- C is the value of the curvature at the moment t.
- K is a fitting parameter.

As previously, the hysteretic behavior is described using the fractional derivative (Eq. 49).

$$M = M_j^{loopi} + B_b \cdot \text{sign}\left(C - C_j^{loopi}\right) \cdot \frac{\Gamma(2)}{\Gamma(2-\alpha)} \cdot \left|C - C_j^{loopi}\right|^{1-\alpha} \tag{49}$$

Where:

- i corresponds to the number of the loop.
- M_j^{loopi} corresponds to the value of the bending moment before the unloading phase or before the ascending phase of a loop (reloading).
- C_j^{loopi} corresponds to the value of the curvature before the unloading phase or before the ascending phase of a loop (reloading).
- α is the derivative order.
- B_b is a fitting coefficient for the orientation of the fractional derivative.
- $j = 0$ if unloading and $j = 1$ if loading (see Fig. 3).

Now that the models are defined, it is necessary to identify their parameters. This is the aim of the following section.

4. Fractional derivatives application

The purpose of this section is to propose different models from the theoretical approaches defined in the previous section. Section 5 describes the protocole to follow to identify every variable.

4.1. Application for in-plane shear behavior

In this section, four models are proposed ranging from the simplest to the most complicated to identify. The first model consists of a dissipative law, with a yield criterion and variables describing the isotropic and kinematic hardening functions. Hysteresis loops are described by linear approaches. The second model takes into account the hysteresis loop only during the unloading. Once the unloading is done, if a reload takes place, it is supposed to be elastic. The third model consists of applying the fractional derivative during unloading but also during reloading in order to completely describe the hysteresis loop. Finally, the fourth model proposes a finer evolution of the parameters describing the fractional derivative in order to have a better description of the experimental curve.

It is however important to specify that the dissipation phase (Eq. (50)) is common to all models and the identified parameters are presented in Table 2.

$$\begin{cases} f_s\left(\gamma_p\right) &= \left|\mu K_{sh}\left(F_{11}F_{21}+F_{12}F_{22}-\sin\left(\gamma_p\right)\right)-\sum_{i=1}^{4}Q_i\gamma_p^i\right|-\left(S_y+\sum_{i=1}^{4}A_i\left|\gamma_p\right|^i\right) \\ E_{e12} &= \frac{1}{2}\cdot\left(F_{11}F_{12}+F_{21}F_{22}-sin\left(\gamma_p\right)\right) \\ S_{12} &= \mu K_{sh}E_{e_{12}} \end{cases} \tag{50}$$

The variables A_i and Q_i are respectively associated with the isotropic and kinematic hardening. More details concerning the identification process are given in [27]. A fourth order polynomial approximation is enough to describe both hardening functions.

In addition, for each model there are four different phases defined below. These four phases take effect as soon as the material has dissipated energy (i.e $\gamma_p \neq 0$). These four phases correspond to four possible configurations:

- Phase 1 denoted P_1: Dissipation in loading, which means $|\gamma|$ evolves and is bigger than the previous shear angle noted $|\gamma^{prev}|$ and γ_p also evolves. This is the upper bound of the experimental result in Fig. 5.
- Phase 2 denoted P_2: Dissipation during unloading, which means $|\gamma|$ evolves and is smaller than the previous shear angle noted $|\gamma^{prev}|$ and γ_p also evolves. This is the lower bound of the experimental result in Fig. 5.
- Phase 3 denoted P_3: unloading phase, which means $|\gamma|$ evolves and is smaller than the previous shear angle noted $|\gamma^{prev}|$ and γ_p is constant. This is the descending phase of a hysteresis loop.
- Phase 4 denoted P_4: reloading phase, which means $|\gamma|$ evolves and is bigger than the previous shear angle noted $|\gamma^{prev}|$ and γ_p is constant. This is the ascending phase of a hysteresis loop.

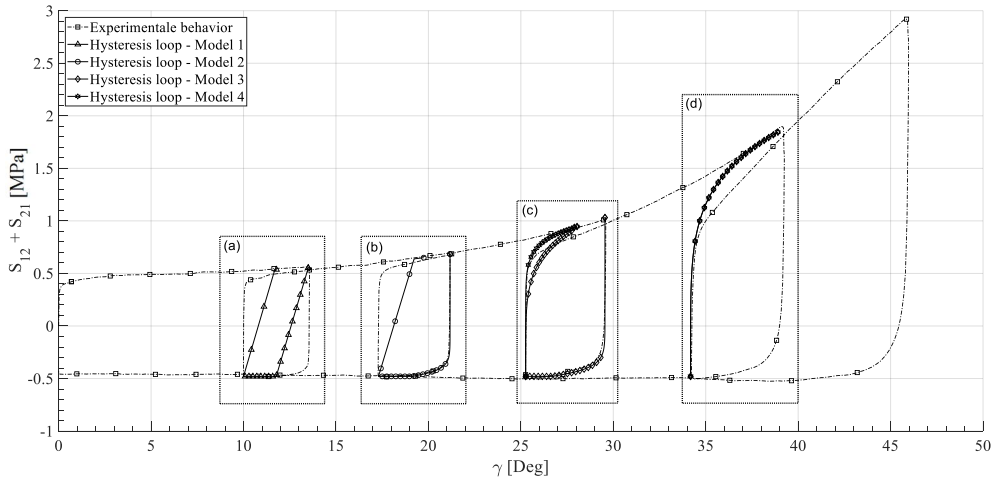

Fig. 7: Different models to simulate the hysteresis loops for a picture frame test under cyclic loading: (a) model 1, (b) model 2, (c) model 3 and 4, (d) model 3 and 4.

The summary of these four phases is defined below.

$$Phase: \begin{cases} P_1 & if \ \ |\gamma| \geq |\gamma^{prev}| \\ P_2 & if \ \ |\gamma| < |\gamma^{prev}| \\ P_3 & if \ \ |\gamma| < |\gamma^{prev}| \ \ and \ \ |\gamma_p| \ \ constant \\ P_4 & if \ \ |\gamma| \geq |\gamma^{prev}| \ \ and \ \ |\gamma_p| \ \ constant \end{cases} \tag{51}$$

The four models presented below take into account these four distinct loading phases.

Model 1 presented in Eq. (52)**.**

With this model only seven simple parameters must be identified and are presented in Table 2. This model makes possible to define the upper and lower bounds of the experimental curve but does not represent the reality of the hysteresis loops. The application of this model is used to describe the first hysteresis loop of Fig. 7(a). This model is very simple, very fast and easily identifiable. It allows a rough approach to the behavior.

$$S_{12} = \begin{cases} K_{sh} E_{e_{12}} & if \ P_1 \\ K_{sh} E_{e_{12}} & if \ P_2 \\ K_{sh} E_{e_{12}} & if \ P_3 \\ K_{sh} E_{e_{12}} & if \ P_4 \end{cases} \tag{52}$$

Model 2 presented in Eq. (53)**.**

This model involving the fractional derivative during the phase P_3 requires some additional parameters. Indeed, the order of the derivative and the fitting term before the fractional derivative must be identified.

Geometrically, the alpha parameter can be considered as the size of the straight part of the loop. This parameter may initially be considered constant. The definition of parameter B_{sh} in Eq. (46) depends on the value of the stress at the beginning of the unloading. Indeed, it is this parameter that guides the fractional derivative to fit with the experimental approach. In order to find this parameter, a simple dichotomy search is sufficient since the result is unique. The ascending part P_4 of the loop is assumed to be linear in this description. This model remains relatively simple and it is easier to identify than more sophisticated models. The identification method and protocol are described in section 5. The use of the derivative in the sense of Caputo takes all its interest here since no numerical approximation (Simpsons, Gauss or other) had to be made. A gain in accuracy and time is therefore considerable. This model corresponds to the second hysteresis loop shown in Fig. 7(b).

$$S_{12} = \begin{cases} K_{sh} E_{e_{12}} & if\ P_1 \\ K_{sh} E_{e_{12}} & if\ P_2 \\ \frac{1}{2} S_0^{loopi} + \mu \cdot K_{sh} \cdot \left[\sum_{m=0}^{3} B_{sh}^m \left| S_0 \right|^m \right] \cdot \text{sign} \left(\gamma - \gamma_0^{loopi} \right) \cdot \frac{\Gamma(2)}{\Gamma(2-\alpha)} \cdot \left| \gamma - \gamma_0^{loopi} \right|^{1-\alpha} & if\ P_3 \\ K_{sh} E_{e_{12}} & if\ P_4 \end{cases} \tag{53}$$

The identified parameters for this model are proposed in Table 2. The parameters for the dissipative model are the same as those proposed for model 1.

The model taking into account the fractional derivative phase P3 therefore requires twelve coefficients. This model combines both a fine description for a cycle and remains fairly correct in case of multiple loops while being not very difficult to identify and manipulate. However, in order to be able to be more precise and more reliable, it is possible to write a third model taking into account the ascending phase of the hysteresis loops.

Model 3 presented in Eq. (54).

This model is presented in Eq. (54) and proposed, in addition to model 2, a description of the fractional derivative for the ascending phase of the hysteresis loop (Fig. 7(c, d)).

$$S_{12} = \begin{cases} K_{sh} E_{e_{12}} & if\ P_1 \\ K_{sh} E_{e_{12}} & if\ P_2 \\ \frac{1}{2} S_0^{loopi} + \mu \cdot K_{sh} \cdot \left[\sum_{m=0}^{3} B_{sh}^m \left| S_0 \right|^m \right] \cdot \text{sign} \left(\gamma - \gamma_0^{loopi} \right) \cdot \frac{\Gamma(2)}{\Gamma(2-\alpha)} \cdot \left| \gamma - \gamma_0^{loopi} \right|^{1-\alpha} & if\ P_3 \\ \frac{1}{2} S_1^{loopi} + \mu \cdot K_{sh} \cdot \left[\sum_{n=0}^{3} B_{sh*}^n \left| S_1 \right|^n \right] \cdot \text{sign} \left(\gamma - \gamma_1^{loopi} \right) \cdot \frac{\Gamma(2)}{\Gamma(2-\beta)} \cdot \left| \gamma - \gamma_1^{loopi} \right|^{1-\beta} & if\ P_4 \end{cases} \tag{54}$$

The parameters of model three are presented in Table 2. These parameters complete the previous ones. They remain valid for the P_1, P_2 and P_3 phases.

This model makes possible to describe in addition to the two previous models the ascending phase of the hysteresis loop with seventeen parameters. However, given the evolutionary shape of the upper boundary

that exponentially grows from 40 degrees (Fig. 7), the order of the fractional derivative must be small to avoid going through the upper (or lower) experimental boundary. Thus, identification difficulties may appear to match the experimental curve. An even more evolved model that is more difficult to identify can be described by varying the derivative order as a function of the shear angle. This is the model 4 presented below (Fig. 7(c, d)).

Model 4 presented in Eq. (55)

Model 4 is almost identical to model 3, however, in order to have a closer match with the experimental behavior, an evolution of the derivative order is made in addition to the evolution of the fitting parameter. As a result, it is easier to control the evolution of the model in order to describe the hysteresis loops, whatever the value of the shear angle. The complete model is presented in Eq. (55) and the parameters are shown in Table 2.

$$S_{12} = \begin{cases} K_{sh} E_{e_{12}} & if\ P_1 \\ K_{sh} E_{e_{12}} & if\ P_2 \\ \frac{1}{2} S_0^{loopi} + \mu \cdot K_{sh} \cdot \left[\sum_{m=0}^{3} B_{sh}^{m} \left| S_0 \right|^m \right] \cdot \text{sign}\left(\gamma - \gamma_0^{loopi} \right) \cdot \frac{\Gamma(2)}{\Gamma(2-\alpha)} \cdot \left| \gamma - \gamma_0^{loopi} \right|^{1-\alpha} & if\ P_3 \\ \frac{1}{2} S_1^{loopi} + \ \mu \cdot K_{sh} \cdot \left[\sum_{n=0}^{3} B_{sh*}^{n} \left| S_1 \right|^n \right] \cdot \text{sign}\left(\gamma - \gamma_1^{loopi} \right) \cdot \frac{\Gamma(2)}{\Gamma(2-\beta(\gamma_1))} \cdot \left| \gamma - \gamma_1^{loopi} \right|^{1-\beta(\gamma_1)} & if\ P_4 \end{cases} \tag{55}$$

The evolution of the order of the derivative is not constant and follows a linear function such as presented in Eq. (56).

$$\beta(\gamma_1) = \begin{cases} \beta_{critical} & if\ \ |\gamma| < \gamma_{critical} \\ \beta_1 \left| \gamma_1 \right| + \beta_0 & otherwise \end{cases} \tag{56}$$

With this model, it is necessary to have twenty parameters in order to correctly describe the hysteretic behavior in shear (parameters for the dissipative evolution, the parameters associated to the model 2 and then the parameters for model 4 in Table 2). It is the most complex model and therefore the most difficult to identify. However, it leads to a good numerical approximation of the experimental behavior when multiple cycles appear. In addition, during the forming process, the angles may vary and even change of sign during a variation. As a result, the model must be able to predict the result regardless of the sign of the shear angle. Using model number 3 it is possible to get the result shown in Fig. 7. This simulation proposes a prediction up to a shear angle of 60 degrees maximum which is already very satisfactory. Indeed, it is not common to reach such high angles while draping fibrous material. Moreover, from this angle, locking phenomena appear and thus, coupling between deformation modes takes place. The assumptions previously defined are no longer valid.

Appendix B proposes a Matlab® algorithm to use the model number 2. An algorithm framework is also given in Appendix A.

4.2. Parameters identification for bending behavior

The model proposed in Eqs. (48) and (49) allows to describe the bending behavior. By considering the experimental approach presented in Fig. 3 it is, as for the shearing behavior, possible to describe several phases.

$$Phase: \begin{cases} P_1 & if \ |C| \geq \left|C_j^{loopi}\right| \ or \ |M| > M_{max} \\ P_2 & if \ C < C^{prev} \ and \ |C| \ < \left|C_j^{loopi}\right| \\ P_3 & otherwise \end{cases} \tag{57}$$

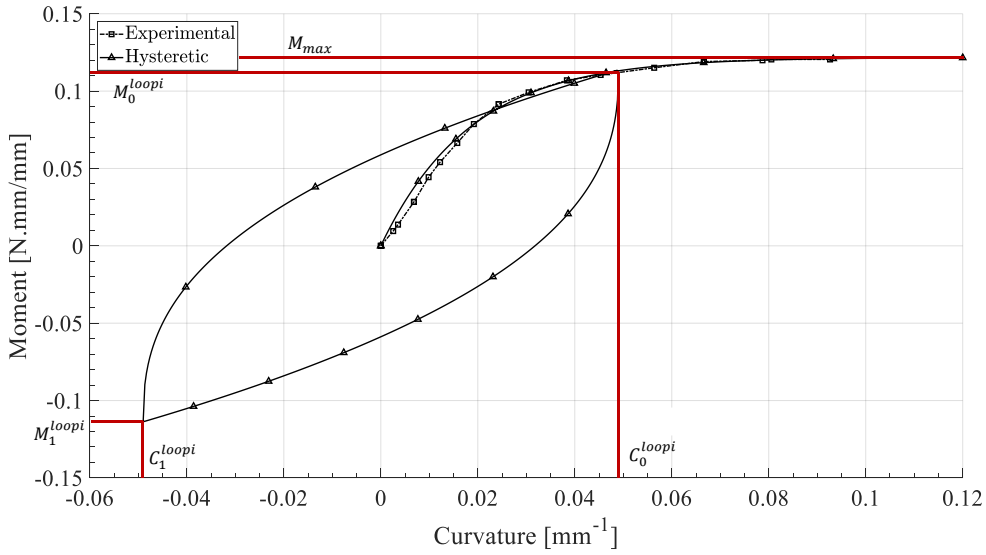

Fig. 8: Bending coefficient related to the proposed model.

Data from the phases presented in Eq. (57) can be founded in Fig. 8. Variable C corresponds to the actual curvature, C^{prev} the curvature at the previous timestep, M the actual bending moment and M_{max} the maximum bending moment reached by the experimental curve. Unlike the in-plane shear model, the aim is to propose the feasibility of the method by applying it in order to have a realistic approximation of the bending behavior. The idea is therefore to fit the experimental behavior proposed in Fig. 3 and assume cyclic behavior corresponding to a Kawabata test as it is often presented in the literature. The associated parameters are presented in Table 3 and correspond to the model presented in Eq. (58). Since this model is purely empirical, the conditions for the phases P_1, P_2, P_3 are slightly different than the phases for the in-plane shear model which are more specific. Indeed, the bending behavior is not at all the same as the in-plane shear one. The absolute value of C_j^{loopi} corresponds to the symmetrical aspect of a Kawabata experiment [33]. This symetry means that between the interval $[-C_j^{loopi}, +C_j^{loopi}]$, the evolution will be hysteretical. Moreover, since during an unloading or realoading phase the moment is calculated by the

hysteretic approach, it is important to check if this calculated moment is not over M_{max}. This precaution is made by this following criterion: $|M| > M_{max}$. As for the in-plane shear mode, the index j is associated to the loading state: $j = 0$ if unloading and $j = 1$ if reloading.

$$M = \begin{cases} M_{max} \cdot \left(1 - \exp\left(-\frac{C}{K}\right)\right) & if\ P_1 \\ M_0^{loopi} + \left[\sum_{\delta=0}^{8} B_b^{\delta} \left|C\right|^{\delta}\right] \cdot \text{sign}\left(C - C_0^{loopi}\right) \cdot \frac{\Gamma(2)}{\Gamma(2-\alpha)} \cdot \left|C - C_0^{loopi}\right|^{1-\alpha} & if\ P_2 \\ M_1^{loopi} + \left[\sum_{\delta=0}^{8} B_b^{\delta} \left|C\right|^{\delta}\right] \cdot \text{sign}\left(C - C_1^{loopi}\right) \cdot \frac{\Gamma(2)}{\Gamma(2-\alpha)} \cdot \left|C - C_1^{loopi}\right|^{1-\alpha} & if\ P_3 \end{cases} \tag{58}$$

The result from simulation with these parameters is presented in Fig. 14. As before, Appendix D proposes a Matlab® algorithm to use this model for cyclic bending simulation. An algorithm framework is also given in Appendix C.

5. Identification

The identification of the models proposed above is not extremely difficult since only eleven variables need to be identified: Seven in-plane shear variables (μ, K_{sh}, A_i, Q_i, S_y, the derivative order (α or β depending on the model) and the fractional derivative coefficients (B_{sh} or B_{sh*} depending on the model)) and four bending variables (M_{max}, K, α, B_b). Each variable is described in sections 5.1 and 5.2. Some of these variables require an experimental curve interpretation, others require the use of identification algorithms such as dichotomy search. The objective of this section is to briefly present the protocols necessary to identify these variables.

5.1. Identification of the variables for the in-plane shear model

The variables required to describe the dissipative shear model are as follows:

- μ: since the models presented here are for a thin material, this variable represents the surface density. However, for simplicity, this variable is supposed to be equal to 1. It can be introduced and the parameters A_i, Q_i and B_{sh} must be updated. This is a supplier parameter directly linked to the material properties.

- K_{sh}: this is the rigidity corresponding to the linear evolution at the beginning of the load. They can be directly read in the experimental curve.

- A_i and Q_i: they are respectively the isotropic and kinematic hardening variables. They are identified following the method described in [27]. In this paper, it is not the same curve but the identification procedure is the same here.

- S_y: this is the elasticity limit corresponding to the end of the linear part. It can be read directly on the experimental curve.

Time [s]	0	50	0
γ **[deg]**	0	39	0

Table 1: Imposed shear angle loading to get the B_{sh} parameter.

- α: this variable corresponds to the size of the linear part which can be visible during the unloading/reloading phase (see fig. 9). It is quickly identified by fitting the numerical model with the experimental curve. This variable is identified for two cases: α for the unloading and β for the reloading phase. It is also the degree of the fractional derivative.

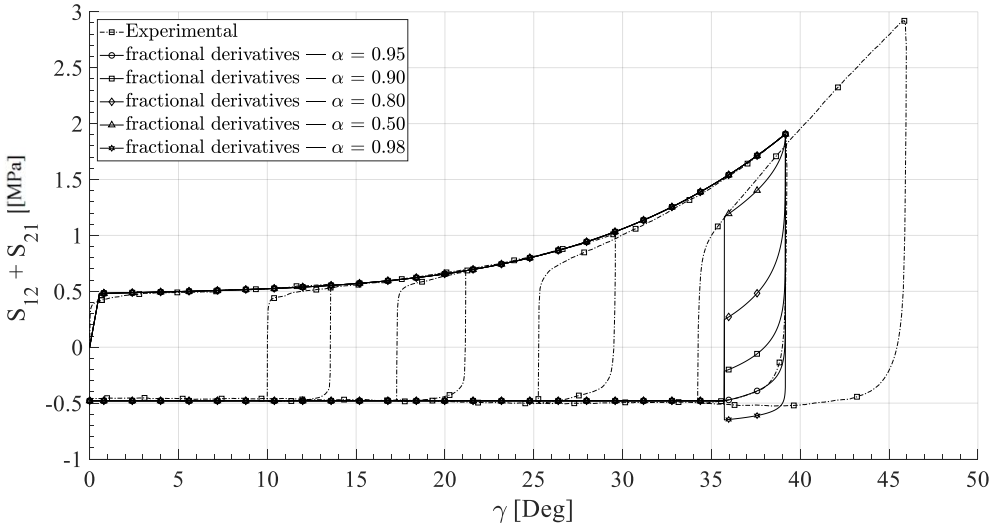

Fig. 9: Different values of the fractional derivative order α and their impact on the related model.

- B_{sh}: as previously, this variable is identified for two cases: B^m_{sh} for the unloading phase or B^n_{sh*} for the reloading phase. A dichotomy algorithm must be applied to identify this variable. Further discussions and details are given below.

Fig. 10 represents the evolution of the variable B_{sh} for the unloading phase (then B^m_{sh}). The protocol consists to give an approximate value of B_{sh} for a given load. Concerning Fig. 10, the imposed load is given in Table 1.

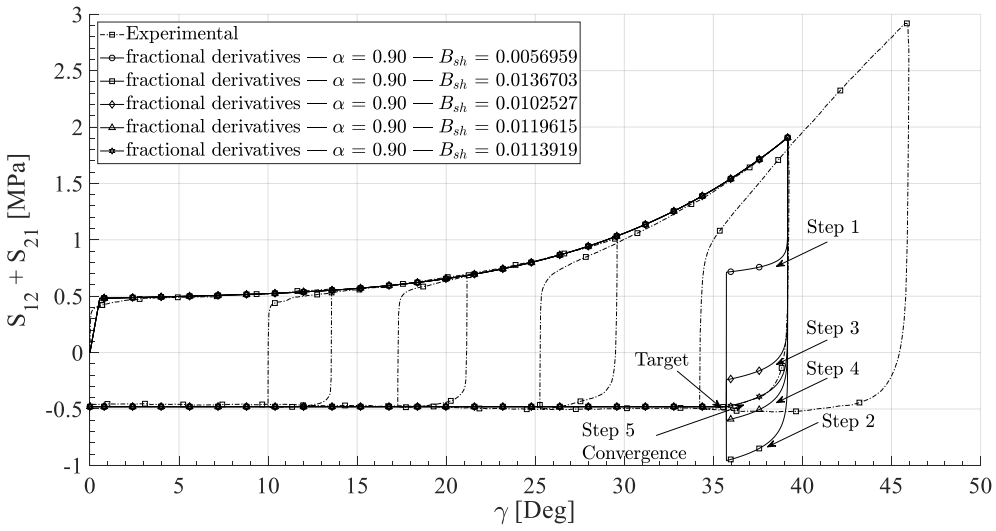

Fig. 10: Evolution of five steps from the dichotomy algorithm.

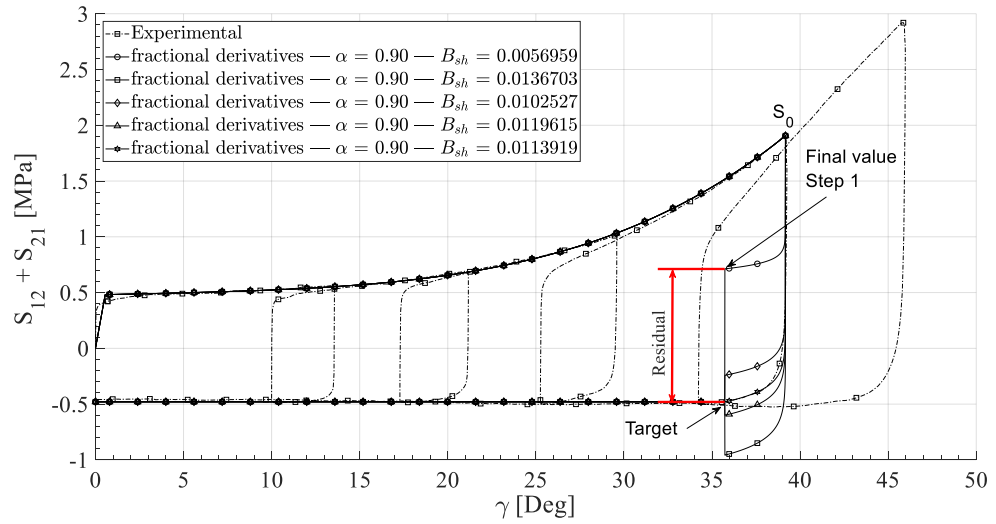

Fig. 11: Illustration of the residual value and the target needed for the dichotomy algorithm.

From an initial value (first value, Step 1 in Fig. 11), it is possible to apply a dichotomy algorithm to reduce the residual presented in Fig. 11. Depending on the sign of the residual, the value for B_{sh} will increase or decrease to finally reach the target considering an error criterion (around 1e-12 here). Usually to find the right value of B_{sh}, it needs five steps. Once the convergence is reached, it is necessary to repeat the operation for another load sligthly different. By this way, it is possible to get the Fig. 12, where each B_{sh} is given for each value of S_0.

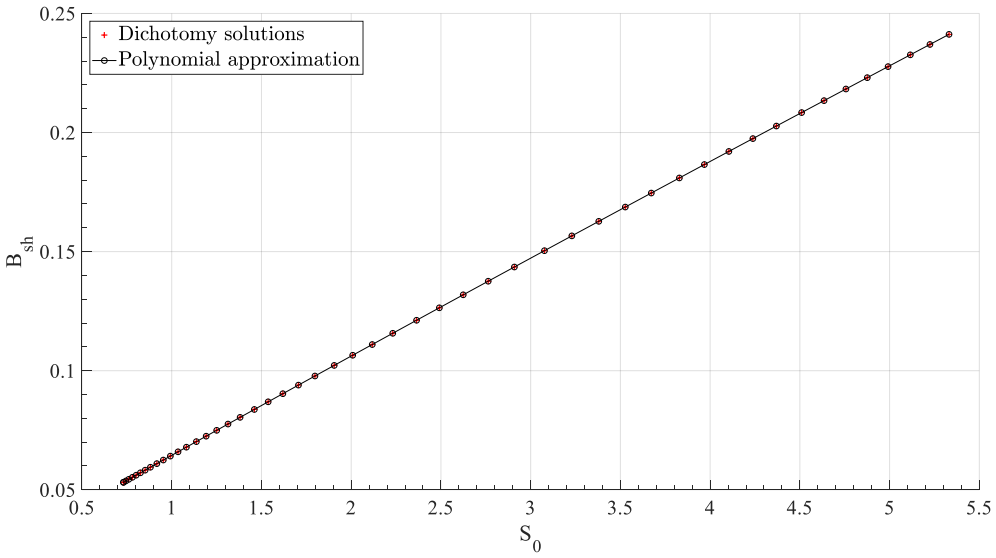

Fig. 12: Approximation in order to find the polynomial coefficients to get the evolution of the parameter B_{sh} as a function of S_0.

Finally, it is possible to describe the evolution of B_{sh} as a function of S_0 by approximating it using a polynomial function. This polynomial needs the parameters B_{sh}^m to describe B_{sh}. The same strategy is applied to define B_{sh*} with the parameters B_{sh*}^n for the reloading phase.

The associated parameters for every variable are given in Table 2. Moreover, a comparison with the first sophisticated model developed presented in [27] is made. Indeed, Fig. 13 compare the experimental data, the Mroz nested surfaces model (presented in [27]) and the fractional derivative approach, model 4. As it is possible to see, the fractional derivatives model suits perfectly well with the experimental behavior. The second interest of the fractional derivatives lies in the number of variables to be identified. The Mroz theory needs a considerable amount of parameters (more than fifty) to identify every variable.

Dissipative evolution parameters for phases P_1 and P_2 - models 1, 2, 3 and 4								
Par.	K_{sh}	$A_1 \mid Q_1$	$A_2 \mid Q_2$	$A_3 \mid Q_3$	$A_4 \mid Q_4$	S_y	μ	-
Val.	50	0.1020	-0.0214	0.5132	2.2415	0.4794	1	-
Parameters for phase P_3 - models 2, 3 and 4								
Par.	α	B^0_{sh}	B^1_{sh}	B^2_{sh}	B^3_{sh}	-	-	-
Val.	0.95	0.00608150	0.01116617	-1.8983E-04	9.3262E-06	-	-	-
Parameters for phase P_4 - model 3 only								
Par.	β	B^0_{sh*}	B^1_{sh*}	B^2_{sh*}	B^3_{sh*}	-	-	-
Val.	0.40	0.099863	-0.0021389	3.4951E-04	-2.7219E-05	-	-	-
Parameters for phase P_4 - model 4 only								
Par.	β_0	β_1	B^0_{sh*}	B^1_{sh*}	B^2_{sh*}	B^3_{sh*}	$\gamma_{critical}$	$\beta_{critical}$
Val.	1.6879	-1.6398	0.01556	-0.0019254	3.3985E-04	-2.4439E-06	0.453	0.95

Table 2: Parameters identified for the models associated with the in-plane shear (Par.: Parameters, Val.: Value).

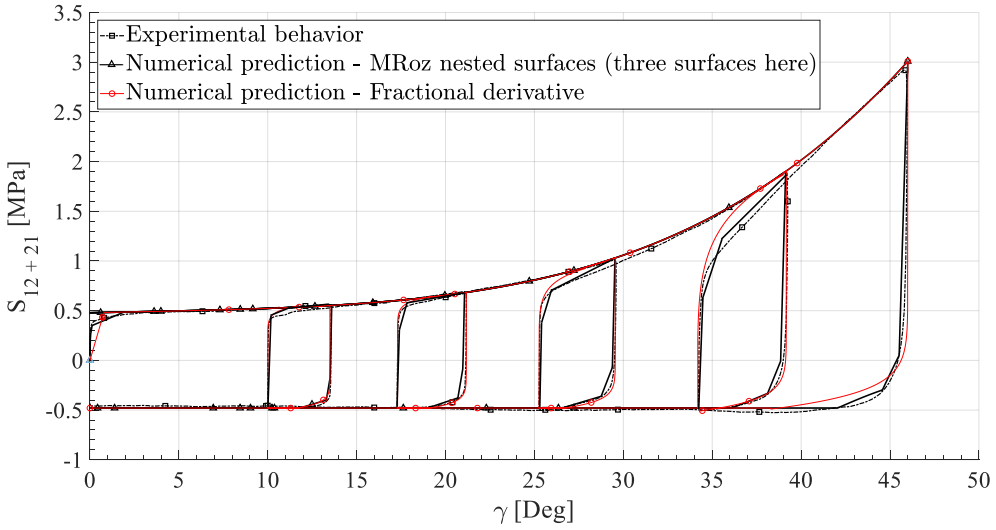

Fig. 13: Comparison between experimental and numerical approaches of a Picture Frame Test under cyclic loading.

5.2. Identification of the variables for the bending model

The variables required to describe the dissipative out of plane bending are the following:

Dissipative evolution parameters						
Par.	M_{max}	K	α	B_b^0	B_b^1	B_b^2
Val.	0.12	0.0185	0.6	0.345603	16.509639	-517.175926
Par.	B_b^3	B_b^4	B_b^5	B_b^6	B_b^7	B_b^8
Val.	7.504174e+03	-6.305304e+04	3.220819e+05	-9.849992e+05	1.657047e+06	-1.178558e+06

Table 3: Parameter values identified for the model in out of plane bending (Par.: Parameters, Val.: Value).

- M_{max}: corresponds to the maximum bending moment when the evolution is stabilized.
- K: corresponds to the bending rigidity which can be identified by the linear part of the experimental curve.
- α: as for in-plane shear, it corresponds to the linear part once there is an unloading or realoading phase.
- B_b: as for in-plane shear, it corresponds to the orientation of the hysteretical path.

Variables M_{max}, K, α are directly defined to fit the experimental curve. For the variable B_b as for the in-plane shear, the protocol is the same but it is necessary to take into account the return path proposed by Abdul-Ghafour et al. [65, 71]. Every parameters needed to identify the variables above are presented in Table 3. Moreover, Fig. 14 represents the predictive behavior of the bending model.

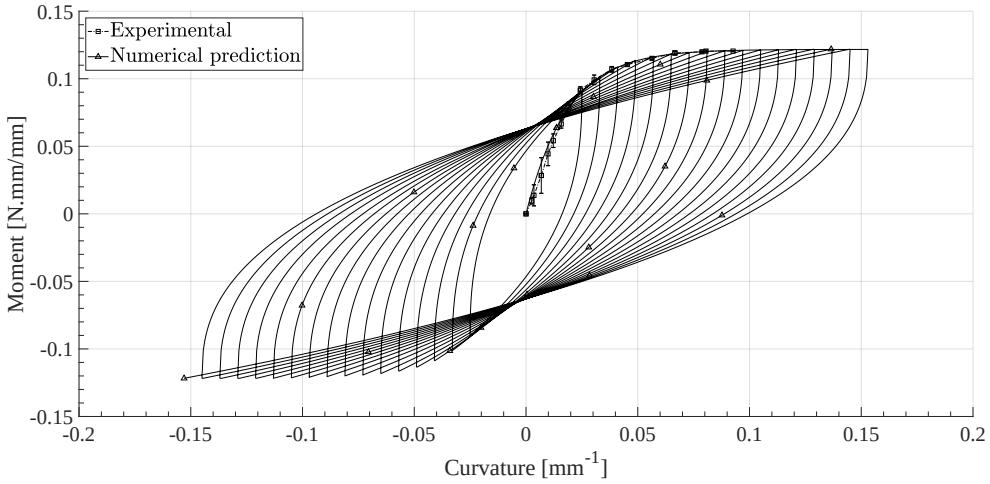

Fig. 14: Numerical result of a cyclical bending test using the fractional derivative approach.

6. Discussions

By integrating these models into a finite element calculation software, simulations of characteristic tests are possible. The simulation results proposed here are from a cyclic bias extension test presented in Fig. 15 [72, 73]. A bias extension test, once deformed, leads to three distinct shear zones which are:

- A fully sheared zone: Zone Z_A in Fig. 15(b)
- Four half-sheared zones: Zones Z_B in Fig. 15(b)
- Zones without shear angle: Zone Z_C in Fig. 15(b)

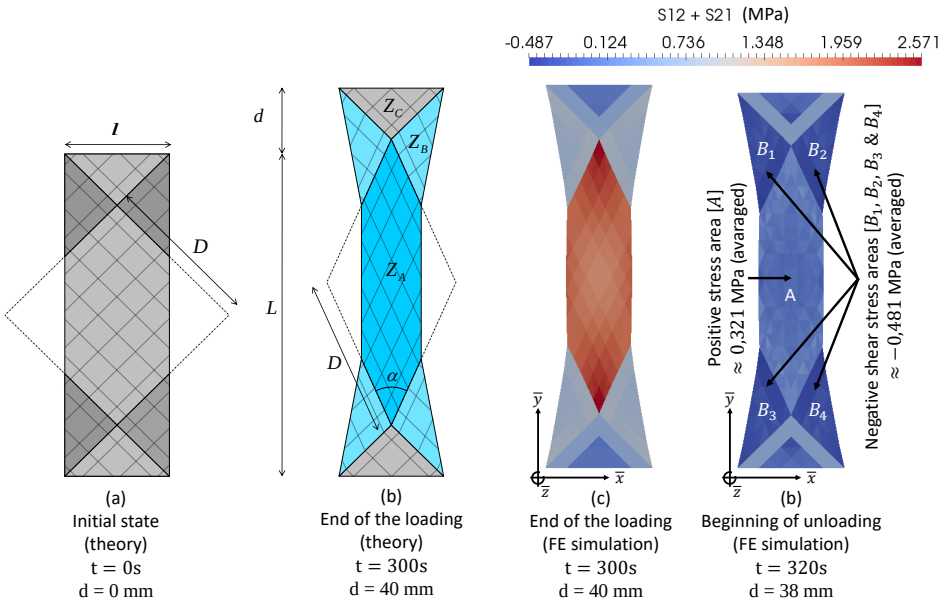

Fig. 15: Bias Extension Test on Hexcel® G1151 dry fabric under cyclic loading: (a) initial state, (b) end of the loading phase (theory), (c) end of the loading phase (simulation), (d) beginning of the unloading phase (simulation).

Considering the evolution of the stress as a function of time during this test with an irreversible model, several interesting phenomena are visible. Firstly, half sheared areas (zones B_1, B_2, B_3 and B_4 in Fig. 15(d)) get a negative shear stress before the main area (zone A in Fig. 15(d)). The close-up part in Fig. 16 shows this phenomenon. Secondly, it is also shown in Fig. 16 that the predicted applied load still remains positive even though the stress in half sheared parts is negative. This interesting effect tends to generate bending dissipation and thus wrinkles may appear (Fig. 17(b-c)).

Continuing unloading, it is possible to see wrinkles at the partially sheared areas (Fig 17(b)) and thus an energy dissipation competition between the bending and the shear makes the wrinkle bigger. Finally, a

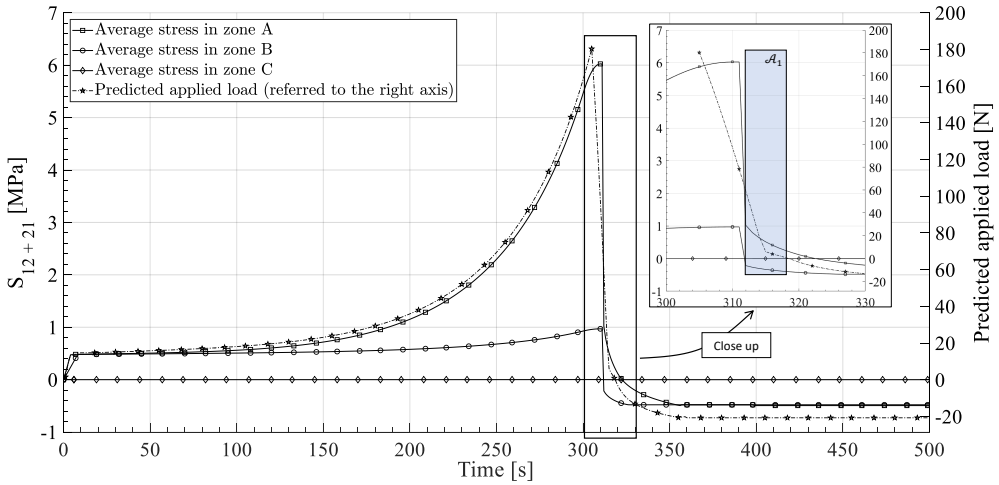

Fig. 16: Temporal evolution of the internal stresses in the different Bias Extension Test areas and evolution of the applied load.

general buckling of the specimen takes place which leads to a out of plane deformation (Fig. 17(c)). A comparison between the hysteretical simulation and an experiment is made in Fig. 17(d). As it is possible to see, the final simulated macroscopic geometry fits with the final experimental geometry. Moreover, this phenomenon appears before having had time to return to the initial position. In fig. 16, in the area A_1 it is possible to see that the half-sheared zones are already under compression while the general strength is still positive. This is a very important result since it shows that new phenomena can be considered. Indeed, with a hyperelastic model, this specific evolution does not appear. (In Fig. 17 and Fig. 19, a comparison between both models is made and the difference is clearly visible). Then, during a forming process simulation, if cyclic loading appears, it is necessary to take into account this hysteretic behavior (further investigations are made later).

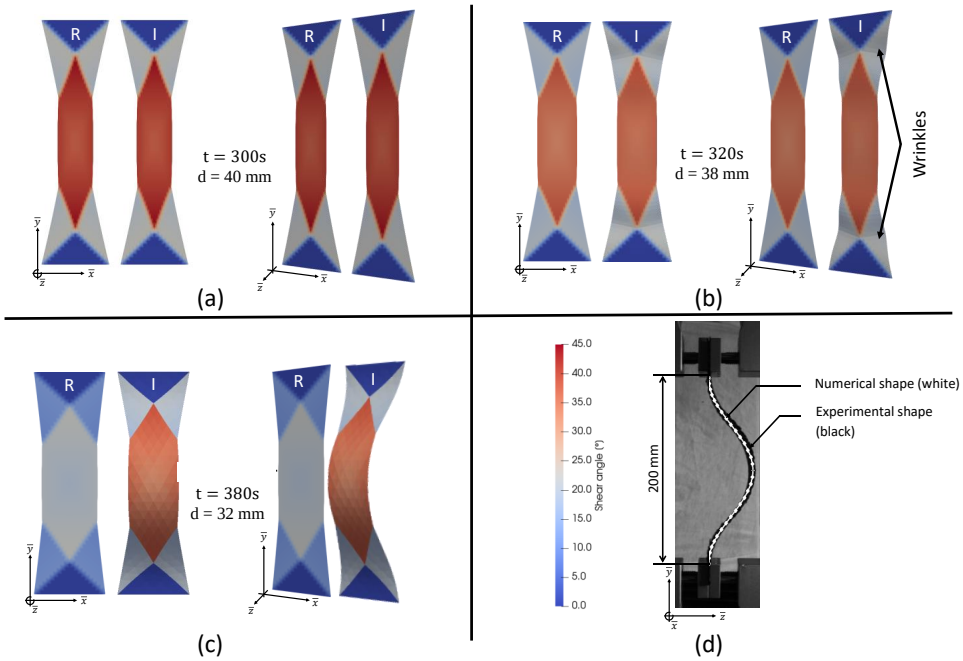

Fig. 17: Comparison of the hyperelastic (denoted by R) and hysteretic (denoted by I) approches in the case of Bias-Extension Test: (a) end of the loading, final shear angle field, (b) beginning of the unloading, (c) end of the unloading, (d) comparison between the hysteretic macroscopic shape and the experiment.

However, even if the fractional derivative approach leads to a good result, it needs precautions concerning the parameters precision. Indeed, as it can be seen in Table 2 and Table 3, the parameters must be precise. The fractional derivative is a very sensitive method and precautions must be taken to avoid identification issues. As it is possible to see in Fig. 18, a small variation of B_{sh} leads to a discontinuity between the hysteresis loop and the dissipative evolution. Therefore, it is important to be precautious with this variable and being precise concerning its value. If B_{sh} is too high, the hysteresis loop will be below the beginning of the dissipative evolution. If B_{sh} is too low, the hysteresis loop will finish above the dissipative evolution. In any case, this discontinuity will lead to numerical perturbation. This model can finally be used in a finite element calculation code in order to be able to simulate forming processes taking into account load variations whether in shear or bending. This is of major importance since the geometries of parts and molds are becoming more and more complex, and the rates higher.

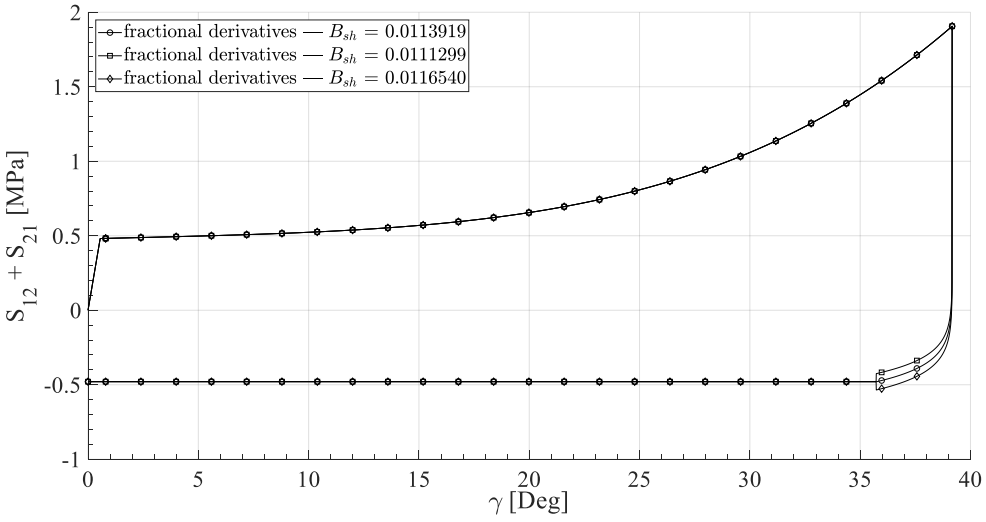

Fig. 18: Analysis of the sensitivity of the parameter B_{sh} for a constant fractional derivative order α. Here, $\alpha = 0.95$.

To conclude this part of the discussion, an illustration of the remarks made previously was obtained by comparing a hyperelastic model, the hysteretic model and an experimental approach in a complex cross-shaped geometry. Fig. 19 illustrates this confrontation. In this figure, it is possible to see two phenomena:

- First, it is clearly visible that the hyperelastic model does not correctly simulate the macroscopic shape and the final orientation of fibres for complex geometries. Indeed, the predicted shape in Fig. 19(b) does not correspond to the experimental configuration. Extremely pronounced wrinkle(s) appear in the simulation whereas in the experiment, they are much smoother. On the contrary, using an irreversible or hysteretic model leads to a good description and a better prediction of the woven shape, all along the preforming of the dry fabric. The experimental test was performed six times to quantify the repeatability of the deep drawing.

- Secondly, when the punches are removed, it is possible to see that the woven fabric returns to its initial position with the reversible or hyperelastic model (Fig. 19(d)). The use of a hysteretic model therefore allows access to the residual stress state as well as to plastic strain (Fig. 19(c)). This allows a better description of the shaping processes (Fig. 19(e-f)) considering phenomena neglected in the past. The experimentally measured springback corresponds to the simulated one.

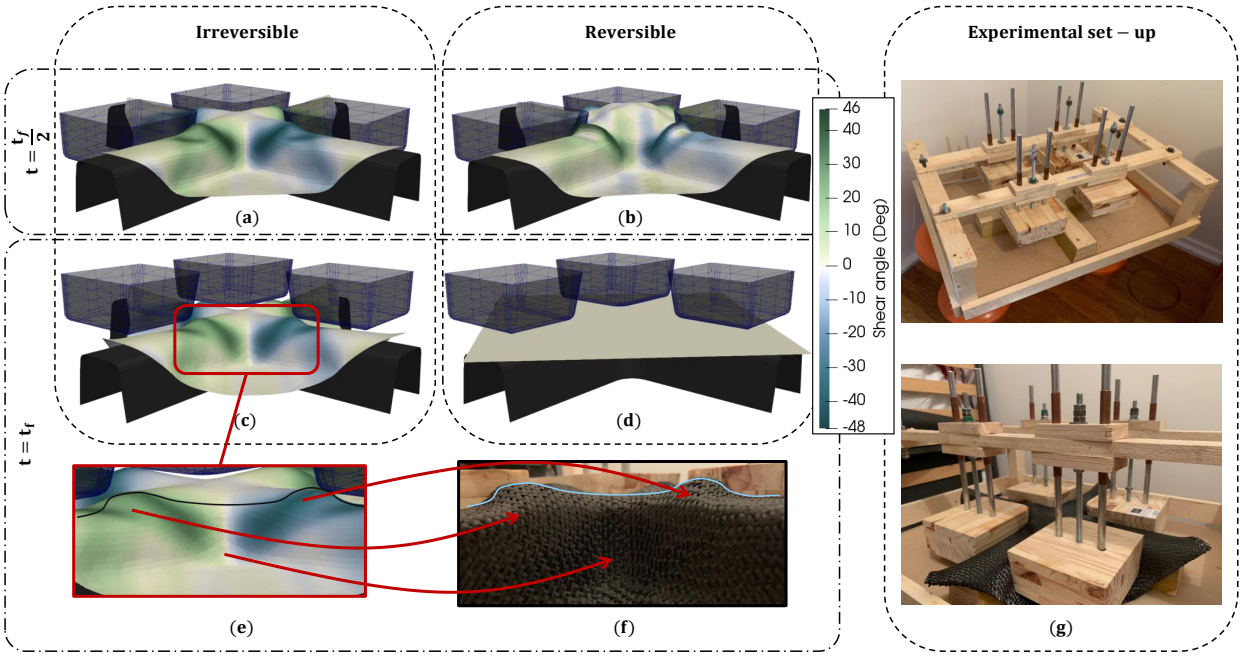

Fig. 19: Deep drawing FE simulation comparison between hyperelastic (reversible), hysteretic appoach (irreversible) and experimental: (a) final state of the woven fabric using an hysteretic model, (b) final state of the woven fabric using an hyperelastic model, (c) elastic return when the punches are removed using an hysteretic model, (d) elastic return when the punches are removed using an hyperelastic model, (e) close up on the irreversible result, (f) close up on the experimental result, (g) experimental set-up.

7. Conclusion

This paper proposes an irreversible constitutive law for in-plane shear and out of plane bending dissipative modes. A fractional derivative approach makes possible to have a very good compromise between the number of parameters, the identification procedure and the quality of the prediction. This also makes possible to have results that are more consistent during the forming simulation of the woven composite materials. The assumptions presented at the beginning of this document are valid for many case studies such as composite thin fabric. Indeed, cyclic loading may appear in bending and shearing and thus the available hyperelastic models were not rich enough to have consistent results between the simulations and the experimental tests. This type of model thus makes possible to answer the current industrial needs and the major innovation of this paper consists in developing complex irreversible models having hysteresis loops without requiring many parameters as might be required by some previously established models.

However, establish such a model which makes possible to solve problems of irreversible phenomena, leads to other perspectives and other questions. For example, it is now possible to show buckling when compressing an already sheared material.

It is also very important to properly calibrate this fractional derivative by identifying the parameters. Indeed, this method is very sensitive, a minimal variation in the identified parameters can generate strong instabilities in the calculation. It is therefore often necessary to have detailed parameters. This model allows both a better representation of physical phenomena while being easy to apply. Indeed, even if the variables are quite sensitive, the identification procedure does not need a lot of time and effort. This method also opens up new perspectives for further work.

To conclude this paper, the models presented are calibrated by doing a Picture Frame Test or Bending test under cyclical loading. To validate the models, a bias extension was also made, and it is shown that this model makes possible to simulate the buckling effect that appear when the BET Sample undergoes unloading. In both cases, the model leads to a good description of the experiments. Furthermore, a concise comparison was made concerning a deep drawing, but no quantitative data are for now published. The idea was to validate the model by doing a macroscopic or qualitative approach only. For now, and from the author knowledge, there is no literature where such model is presented and compared to complex geometry forming. Since new process strategies are emerging such as incremental forming, this paper was made to answer some problematic linked to these new strategies by proposing a model capable to describe the hysteresis loops.

8. Bibliography

[1] F. Trochu, R. Gauvin, D.-M. Gao, Numerical analysis of the resin transfer molding process by the finite element method, Advances in Polymer Technology: Journal of the Polymer Processing Institute 12 (4) (1993) 329–342.

[2] T. S. Lundström, B. R. Gebart, Influence from process parameters on void formation in resin transfer molding, Polymer Composites 15 (1) (1994) 25–33.

[3] D. Rouison, M. Sain, M. Couturier, Resin transfer molding of natural fiber reinforced composites: cure simulation, Composites science and technology 64 (5) (2004) 629–644.

[4] P. Ladevéze, G. Lubineau, On a damage mesomodel for laminates: micro–meso relationships, possibilities and limits, Composites Science and Technology 61 (15) (2001) 2149–2158.

[5] P. Ladevèze, F. Daghia, E. Abisset, C. Le Mauff, A micromechanics-based interface mesomodel for virtual testing of laminated composites, Advanced Modeling and Simulation in Engineering Sciences 1 (1) (2014) 7.

[6] P. Ladevèze, O. Allix, J.-F. Deü, D. Lévêque, A mesomodel for localisation and damage computation in laminates, Computer methods in applied mechanics and engineering 183 (1-2) (2000) 105–122.

[7] G. J. Dvorak, Composite materials: Inelastic behavior, damage, fatigue and fracture, International Journal of Solids and Structures 37 (1-2) (2000) 155–170.

[8] C. Hochard, P.-A. Aubourg, J.-P. Charles, Modelling of the mechanical behaviour of woven-fabric cfrp laminates up to failure, Composites Science and Technology 61 (2) (2001) 221–230.

[9] C. Hochard, J. Payan, O. Montagnier, Design and computation of laminated composite structures, Composites science and technology 65 (3-4) (2005) 467–474.

[10] L. Lozano-Sánchez, A. Sustaita, M. Soto, S. Biradar, L. Ge, E. Segura-Cárdenas, J. Diabb, L. Elizalde, E. Barrera, A. Elías-Zúñiga, Mechanical and structural studies on single point incremental forming of polypropylene-mwcnts composite sheets, Journal of Materials Processing Technology 242 (2017) 218 – 227. doi:https://doi.org/10.1016/j.jmatprotec.2016.11.032.

[11] C. Raju, C. S. Narayanan, Application of a hybrid optimization technique in a multiple sheet single point incremental forming process, Measurement 78 (2016) 296 – 308. doi:https://doi.org/10.1016/j.measurement.2015.10.025.

[12] T. McAnulty, J. Jeswiet, M. Doolan, Formability in single point incremental forming: A comparative analysis of the state of the art, CIRP Journal of Manufacturing Science and Technology 16. doi:10.1016/j.cirpj.2016.07.003.

[13] S. Coutandin, D. Brandt, P. Heinemann, P. Ruhland, J. Fleischer, Influence of punch sequence and prediction of wrinkling in textile forming with a multi-punch tool, Production Engineering 12 (6) (2018) 779–788. doi:10.1007/s11740-018-0845-9.

[14] H. Peng, H. Liu, X. Zhang, Numerical investigation of wrinkle for multi-point thermoforming of polymethylmethacrylate sheet, IOP Conference Series: Materials Science and Engineering 242 (2017) 012028. doi:10.1088/1757-899x/242/1/012028.

[15] X. Peng, Z. Guo, T. Du, W.-R. Yu, A simple anisotropic hyperelastic constitutive model for textile fabrics with application to forming simulation, Composites Part B: Engineering 52 (2013) 275–281.

[16] A. Charmetant, J. G. Orliac, E. Vidal-Sallé, P. Boisse, Hyperelastic model for large deformation analyses of 3d interlock composite preforms, Composites Science and Technology 72 (12) (2012) 1352–1360.

[17] S. Dridi, A. Dogui, P. Boisse, Finite element analysis of bias extension test using an orthotropic hyperelastic continuum model for woven fabric, Journal of the Textile Institute 102 (9) (2011) 781–789.

[18] Y. Aimene, B. Hagege, F. Sidoroff, E. Vidal-Sallé, P. Boisse, S. Dridi, Hyperelastic approach for composite reinforcement forming simulations, International Journal of Material Forming 1 (1) (2008) 811–814.

[19] X. Peng, Z. Guo, P. Harrison, et al., A simple anisotropic fiber reinforced hyperelastic constitutive model for woven composite fabrics, International journal of material forming 3 (1) (2010) 723–726.

[20] L. Liu, J. Chen, X. Li, J. Sherwood, Two-dimensional macro-mechanics shear models of woven fabrics, Composites Part A: Applied science and manufacturing 36 (1) (2005) 105–114.

[21] G. A. Holzapfel, T. C. Gasser, A viscoelastic model for fiber-reinforced composites at finite strains: continuum basis, computational aspects and applications, Computer methods in applied mechanics and engineering 190 (34) (2001) 4379–4403.

[22] P. Harrison, M. Clifford, A. Long, Shear characterisation of viscous woven textile composites: a comparison between picture frame and bias extension experiments, Composites Science and Technology 64 (10) (2004) 1453–1465.

[23] E. Guzman-Maldonado, N. Hamila, N. Naouar, G. Moulin, P. Boisse, Simulation of thermoplastic prepreg thermoforming based on a visco-hyperelastic model and a thermal homogenization, Materials & Design 93 (2016) 431–442.

[24] E. Guzman-Maldonado, N. Hamila, P. Boisse, J. Bikard, Thermomechanical analysis, modelling and simulation of the forming of pre-impregnated thermoplastics composites, Composites Part A: Applied Science and Manufacturing 78 (2015) 211–222.

[25] Y. Gong, X. Peng, Y. Yao, Z. Guo, An anisotropic hyperelastic constitutive model for thermoplastic woven composite prepregs, Composites Science and Technology 128 (2016) 17–24.

[26] A. Krasnobrizha, P. Rozycki, L. Gornet, P. Cosson, Hysteresis behaviour modelling of woven composite using a collaborative elastoplastic damage model with fractional derivatives, Composite Structures 158 (2016) 101–111.

[27] Y. Denis, E. Guzman-Maldonado, N. Hamila, J. Colmars, F. Morestin, A dissipative constitutive model for woven composite fabric under large strain, Composites Part A: Applied Science and Manufacturing 105 (2018) 165–179.

[28] S. Coutandin, D. Brandt, P. Heinemann, P. Ruhland, J. Fleischer, Influence of punch sequence and prediction of wrinkling in textile forming with a multi-punch tool, Production Engineering 12 (6) (2018) 779–788.

[29] C. Krogh, J. A. Glud, J. Jakobsen, Modeling the robotic manipulation of woven carbon fiber prepreg plies onto double curved molds: A path-dependent problem, Journal of Composite Materials 53 (15) (2019) 2149–2164.

[30] S. Allaoui, G. Hivet, A. Wendling, D. Soulat, S. Chatel, Experimental approach for optimizing dry fabric formability, in:

14th European Conference on Composite Materials, Budapest, Hungary, 2010, pp. ID347–ECCM14.

[31] A. Aridhi, M. Arfaoui, T. Mabrouki, N. Naouar, Y. Denis, M. Zarroug, P. Boisse, Textile composite structural analysis taking into account the forming process, Composites Part B: Engineering 166 (2019) 773–784.

[32] C. Mitchell, L. Dangora, C. Bielmeier, J. Sherwood, Investigation into the changes in bending stiffness of a textile reinforced composite due to in-plane fabric shear: Part 1–experiment, Composites Part A: Applied Science and Manufacturing 85 (2016) 94–102.

[33] E. De Bilbao, D. Soulat, G. Hivet, A. Gasser, Experimental study of bending behaviour of reinforcements, Experimental Mechanics 50 (3) (2010) 333–351.

[34] L. Montero, S. Allaoui, G. Hivet, Characterisation of the mesoscopic and macroscopic friction behaviours of glass plain weave reinforcement, Composites Part A: Applied Science and Manufacturing 95 (2017) 257–266.

[35] G. H. Philippe Boisse, Jean Launay, Experimental analysis of the influence of tensions on in plane shear behaviour of woven composite reinforcements, ScienceDirect, 2010.

[36] I. Podlubny, Fractional differential equations: an introduction to fractional derivatives, fractional differential equations, to methods of their solution and some of their applications, Vol. 198, Elsevier, 1998.

[37] K. S. Miller, B. Ross, An introduction to the fractional calculus and fractional differential equations, 1993.

[38] F. Riewe, Mechanics with fractional derivatives, Physical Review E 55 (3) (1997) 3581.

[39] K. Oldham, J. Spanier, The fractional calculus theory and applications of differentiation and integration to arbitrary order, Vol. 111, Elsevier, 1974.

[40] R. L. Bagley, P. J. Torvik, On the fractional calculus model of viscoelastic behavior, Journal of Rheology 30 (1) (1986) 133–155.

[41] P. Cosson, J. C. Michon, Identification by a non-integer order model of the mechanical behaviour of an elastomer, Chaos, Solitons & Fractals 7 (11) (1996) 1807–1824.

[42] A. C. Galucio, J.-F. Deü, R. Ohayon, A fractional derivative viscoelastic model for hybrid active-passive damping treatments in time domain-application to sandwich beams, Journal of Intelligent Material Systems and Structures 16 (1) (2005) 33–45.

[43] A. C. Galucio, J.-F. Deü, S. Mengué, F. Dubois, An adaptation of the gear scheme for fractional derivatives, Computer methods in applied mechanics and engineering 195 (44-47) (2006) 6073–6085.

[44] J.-F. Deü, A. C. Galucio, R. Ohayon, Finite element formulation for a transient dynamic analysis of viscoelastic beams using fractional derivative constitutive equations, in: Proc. VII International Conference on Computational Plasticity (CD-ROM), Barcelona, Spain, 2003.

[45] N. Heymans, J.-C. Bauwens, Fractal rheological models and fractional differential equations for viscoelastic behavior, Rheologica acta 33 (3) (1994) 210–219.

[46] R. Koeller, Applications of fractional calculus to the theory of viscoelasticity, Journal of Applied Mechanics 51 (2) (1984) 299–307.

[47] T. F. Nonnenmacher, R. Metzler, On the riemann-liouville fractional calculus and some recent applications, Fractals 3 (03) (1995) 557–566.

[48] H. Schiessel, A. Blumen, Hierarchical analogues to fractional relaxation equations, Journal of Physics A: Mathematical and General 26 (19) (1993) 5057.

[49] M. Caputo, F. Mainardi, A new dissipation model based on memory mechanism, Pure and applied Geophysics 91 (1) (1971) 134–147.

[50] R. L. Bagley, P. Torvik, A theoretical basis for the application of fractional calculus to viscoelasticity, Journal of Rheology 27 (3) (1983) 201–210.

[51] A. C. Galucio, J.-F. Deü, R. Ohayon, Finite element formulation of viscoelastic sandwich beams using fractional derivative

operators, Computational Mechanics 33 (4) (2004) 282–291.
[52] A. C. Galucio, J.-F. Deü, S. Mengué, F. Dubois, An adaptation of the Gear scheme for fractional derivatives, Computer Methods in Applied Mechanics and Engineering 195 (44-47) (2006) 6073–6085. doi:10.1016/j.cma.2005.10.013.
[53] M. H. Kashani, A. Rashidi, B. Crawford, A. Milani, Analysis of a two-way tension-shear coupling in woven fabrics under combined loading tests: Global to local transformation of non-orthogonal normalized forces and displacements, Composites Part A: Applied Science and Manufacturing 88 (2016) 272–285.
[54] M. H. Kashani, A. Hosseini, F. Sassani, F. Ko, A. Milani, Understanding different types of coupling in mechanical behavior of woven fabric reinforcements: A critical review and analysis, Composite Structures 179 (2017) 558–567.
[55] C. Mitchell, L. Dangora, C. Bielmeier, J. Sherwood, Investigation into the changes in bending stiffness of a textile reinforced composite due to in-plane fabric shear: Part 2–numerical analysis, Composites Part A: Applied Science and Manufacturing 85 (2016) 138–147.
[56] Z. MRoz, On the description of anisotropic workhardening, Journal of Mechanic, Physics. Solids, 1967.
[57] H. Ziegler, The Theory of Plasticity : A Survey of Recent Achievements, James Clayton Lecture, 1955.
[58] H. Ziegler, A modification of Prager's hardening rule, Brown University, pp: 55-65, 1959.
[59] K. S. Miller, The weyl fractional calculus, in: Fractional calculus and its applications, Springer, 1975, pp. 80–89.
[60] M. Caputo, M. Fabrizio, A new definition of fractional derivative without singular kernel, Progr. Fract. Differ. Appl 1 (2) (2015) 1–13.
[61] E. Hille, R. S. Phillips, Functional analysis and semi-groups, Vol. 31, American Mathematical Soc., 1996.
[62] S. Kawabata, M. Niwa, H. Kawai, Finite-deformation theory of plain-weave fabrics - 3. the shear-deformation theory, Journal of the textile institute 64 (2) (1973) 62–85.
[63] S. V. Lomov, A. Willems, I. Verpoest, Y. Zhu, M. Barburski, T. Stoilova, Picture frame test of woven composite reinforcements with a full-field strain registration, Textile Research Journal 76 (3) (2006) 243–252.
[64] X. Peng, J. Cao, J. Chen, P. Xue, D. Lussier, L. Liu, Experimental and numerical analysis on normalization of picture frame tests for composite materials, Composites Science and Technology 64 (1) (2004) 11–21.
[65] T. A. Ghafour, J. Colmars, P. Boisse, The importance of taking into account behavior irreversibilities when simulating the forming of textile composite reinforcements, Composites Part A: Applied Science and Manufacturing 127 (2019) 105641. doi:https://doi.org/10.1016/j.compositesa.2019.105641.
[66] E. Kroner, (allgemeine kontinuumstheorie der versetzungen und eigenspannungen), archive for rational mechanics and analysis, vol. 4, pp. 273-334 (1960). appendix: Remark on the fundamental geometric law of the general continuum theory of dislocations and initial, Continuum mechanics 1 (1965) 217.
[67] E. H. Lee, Elastic-plastic deformation at finite strains, ASME, 1969.
[68] J. C. Simo, A framework for finite strain elastoplasticity based on maximum plastic dissipation and the multiplicative decomposition: Part i. continuum formulation, Computer methods in applied mechanics and engineering 66 (2) (1988) 199–219.
[69] J. Simo, M. Ortiz, A unified approach to finite deformation elastoplastic analysis based on the use of hyperelastic constitutive equations, Computer methods in applied mechanics and engineering 49 (2) (1985) 221–245.
[70] J. C. Simo, T. J. Hughes, Computational inelasticity, Vol. 7, Springer Science & Business Media, 2006.
[71] T. A. Ghafour, J. Colmars, P. Boisse, The importance of taking into account behavior irreversibilities when simulating the forming of textile composite reinforcements, Composites Part A: Applied Science and Manufacturing 127 (2019) 105641.
[72] P. Boisse, N. Hamila, E. Guzman-Maldonado, A. Madeo, G. Hivet, F. Dell'Isola, The bias-extension test for the analysis of in-plane shear properties of textile composite reinforcements and prepregs: a review, International Journal of Material Forming 10 (4) (2017) 473–492.
[73] B. P. Cao J., Akkerman R., Characterization of mechanical behavior of woven fabrics : Experimental methods and

benchmark results, Composites Part A : Applied Science and Manufacturing, p. 1037-1053, 2008.

Appendix A. Algorithm framework for in-place shear

Input :

F: Imposed load

$\mathbf{F}_p$: Dissipative contribution imposed by the pure shear kinematics

γ: Calculated from usual anisotropic invariant I_{412}

Parameters: A_i, Q_i, K_{sh}, α, β, μ, S_y, B^m_{sh}, B^n_{sh}, B^n_{sh*}, $\beta_{0,1}$

Initial vectors: $\overline{G}_2$, $\overline{G}_1$

Newton - Raphson paremeters: Iter, IterMax

Output :

S : Piola - Kirchhoff II tensor

γ_p : Dissipative contribution of the shear angle

Steps (for each t = 1, ..., $\mathbf{T_f}$):

1. Calculate the shear angle from **F**: $\gamma = \overline{G}_2 \cdot \mathbf{F}^t\mathbf{F} \cdot \overline{G}_1$
2. Update tensors : $\mathbf{F}_p$, **E**, $\mathbf{E}_p$, $\mathbf{E}_e$
3. Do the elastic prediction : **S**, f_s
4. Different cases may appear :

   if $f_s > 0$: Energy dissipation, while $f_s > 0$, $\gamma_p = \gamma_p$ - $\frac{f_s}{df_s}$, with $df_s = \frac{df_s}{d\gamma_p}$

   Once γ_p found such as $f_s = 0$, update tensors, calculate B_{sh} and B_{sh*} and save $S_{0,1}$, $\gamma_{0,1}$

   if $f_s < 0$: Elastic or hysteretic behavior depending on the model 1, 2, 3 or 4

   if $\gamma_p = 0$: Elasticity, skip

   if $\gamma_p \neq 0$ and $|\gamma| < |\gamma^{prev}|$, apply phase P3 of the chosen model

   if $\gamma_p \neq 0$ and $|\gamma| > |\gamma^{prev}|$, apply phase P4 of the chosen model
5. Update tensors
6. Repeat from step 1

Appendix B. Matlab routine for in-plane shear

```
close all; clear all; clc
%Loading table : First line -> Time || Second line -> Shear angle amplitude
load = [0 50 100 150 200 250 300 350 400 450 500 550 600 650 700 750 800 850
        0 -13.5 13.5 -21.17 21.17 -29.55 29.55 -39.17 39.17 -46 46 -50 50 -55 55 -60 60 0];
%Initialize time & parameters
T0 = 0; Tf = 850; dt = 0.01;
Id = [1 0; 0 1]; K1 = 1000; K2 = K1;
Tol = 0.0000000001;  IterMax = 50;
Ksh = 50; alpha = 0.95; g_prec = 0; gam_p = 0;
inc = 0; gam = 0; Iter = 0; mu = 1; Sy = 0.4794;
A = [2.2415 0.5132 -0.0214 0.1020 0]; Q = [2.2415 0.5132 -0.0214 0.1020 0];
p_ca = [9.32633e-06 -1.898259e-04 0.011166 0.0060815];
for time = T0:dt:Tf   %Beginning of the calculation
    %Calculate load at the moment "time"
    if time > 0
        ind = find(time ≤ load(1,:), 1);
        y1 = load(2, ind-1); y2 = load(2, ind);
        x1 = load(1, ind-1); x2 = load(1, ind);
        gam = (((y2 - y1)/(x2 - x1))*time) + y1 - (((y2 - y1)/(x2 - x1))*x1);
    end
    gam = gam*pi/180;
    %Elastic prediction
    Fp = [cos(gam_p/2) sin(gam_p/2); sin(gam_p/2)  cos(gam_p/2)];
    F  = [cos(gam/2)  sin(gam/2); sin(gam/2)  cos(gam/2)];
    E = 0.5*(F'*F-Id); Ep=0.5*(Fp'*Fp-Id); Ee=E-Ep;
    S=mu*[K1*Ee(1,1) Ksh*Ee(1,2); Ksh*Ee(2,1) K2*Ee(2,2)];
    f  = abs(S(1,2) + S(2,1) - sign(gam)*(Q(1)*abs(gam)^4 + Q(2)*abs(gam)^3 + ...
            Q(3)*abs(gam)^2 + Q(4)*abs(gam)^1 + Q(5))) - (A(1)*abs(gam)^4 + ...
            A(2)*abs(gam)^3 + A(3)*abs(gam)^2 + A(4)*abs(gam)^1 + A(5) + 0.4794)
    %Check the case : f>0 -> Dissipation || f<0 -> Elasticity or Hysteresis loop
    if f > 0 %If f > 0 : Dissipation -> Newton Raphson algo to find the value of gam_p
        Iter = 0;
        while abs(f) > Tol && Iter < IterMax
            Iter = Iter + 1;
            dfsg = sign(S(1,2) + S(2,1))*mu*2*Ksh*-0.5*cos(gam_p);
            gam_p = gam_p - f/dfsg;
            Fp = [cos(gam_p/2)  sin(gam_p/2); sin(gam_p/2)  cos(gam_p/2)];
            Ep = 0.5*(Fp'*Fp - Id);        Ee = E - Ep;
            S  = mu*[K1*Ee(1,1) Ksh*Ee(1,2); Ksh*Ee(2,1) K2*Ee(2,2)];
            f  = abs(S(1,2) + S(2,1) - sign(gam)*(Q(1)*abs(gam)^4 + Q(2)*abs(gam)^3 + ...
```

```
                    Q(3)*abs(gam)^2 + Q(4)*abs(gam)^1 + Q(5))) - (A(1)*abs(gam)^4 + ...
                    A(2)*abs(gam)^3 + A(3)*abs(gam)^2 + A(4)*abs(gam)^1 + A(5) + 0.4794)
        end
        decalage = Ee(1,2); gam_0 = gam; %Save data for history of the material when the ...
           hysteresis model will be activated
        ca = p_ca(1)*abs(S(1,2)+S(2,1))^3 + p_ca(2)*abs(S(1,2)+S(2,1))^2 ...
         + p_ca(3)*abs(S(1,2)+S(2,1)) + p_ca(4);
    elseif abs(gam_p) > 0 %Here, phase P3 or P4 (according the article)
        Check_Sign = sign((gam) - abs(g_prec));
        switch Check_Sign
            case -1 %Case of unloading (Phase P3 in the article)
               SG2 = sign((gam-gam_0))*ca*(gamma(2)/(gamma(2-alpha)))*(abs(gam-gam_0)) ...
               ^(1 - alpha) + decalage;
                S  = mu*[K1*Ee(1,1) Ksh*SG2; Ksh*SG2 K2*Ee(2,2)];
        end
    end
    plot_S(inc + 1) = S(1,2);
    plot_gt(inc + 1) = gam;
    inc = inc + 1;   g_prec = gam;
end
plot(plot_gt*180/pi, plot_S)
```

Appendix C. Algorithm framework for out of plane bending

Input:

Curvature C

Parameters: M_{max}, K, α, B_b^{δ}

Output:

Bending moment M

Steps (for each t = 1, ..., $\mathbf{T_f}$):

1. Check if is a loading or an unloading

   if $|C| \geq |C_{0,1}|$ or $|M| \geq M_{max}$

      if $|M| \geq |M_{max}|$ and $|C| \geq |C_{prev}|$ Update bending moment

   else apply phase P1 of the model

   save $C_{0,1}$, $M_{0,1}$ and calculate B_b

   if $C < C_{prev}$ and $|C| \leq |C_{0,1}|$: apply phase P2 of the model

   else apply phase P3 of the model

2. Update data: C_{prev}

3. Repeat from step 1

Appendix D. Matlab routine for bending

```
close all; clear all; clc
load = [0  5    10    15     20   25
        0  0.14 0.085 0.14  −0.15 0.15] ;
t0 = 0; dt = 0.001; tf =25;
Cmax = 0; inc = 0; Mprev = 0; Cprev = 0;
alpha = 0.6; Mm = 0.12172; K = 0.0185;
BbP = [−1.1786E+06 1.657E+06 −9.85E+05 3.2208E+05 −6.3053E+04 7.5042E+03 −517.5926 ...
    16.5096 0.3456];
for time = t0:dt:tf
    inc = inc + 1;
    if time > 0
        ind = find(time ≤ load(1,:), 1);
        y1 = load(2, ind−1); y2 = load(2, ind);
        x1 = load(1, ind−1); x2 = load(1, ind);
        C = (((y2 − y1)/(x2 − x1))*time) + y1 − (((y2 − y1)/(x2 − x1))*x1);
    else
        C = 0;
    end
    if abs(C) ≥ abs(Cmax) || abs(Mprev) > Mm
        if abs(Mprev)≥Mm && abs(C)≥abs(Cprev)
            M = sign(C)*Mm;
        else
            M = sign(C)*Mm*(1−exp(−abs(C)/K));
        end
        Mloop0 = M; C0 = C; Cmax = C; Mloop1 = M; C1 = C; Bb = 0;
        for Bd = 1:1:length(BbP)
            Bb = Bb + BbP(Bd)*abs(C).^(length(BbP)−Bd);
        end
    elseif (C) < (Cprev) && abs(C) < abs(Cmax)
        M = Mloop0 + Bb*sign(C−C0)*(gamma(2)/gamma(2−alpha))*abs(C−C0)^(1− alpha);
        Mloop1 = M; C1 = C;
    else
        M = Mloop1 + Bb*sign(C−C1)*(gamma(2)/gamma(2−alpha))*abs(C−C1)^(1− alpha);
        Mloop0 = M; C0 = C;
    end
    Cprev = C; Mprev = M;
    plotM(inc,1) = M; plotC(inc,1) = C;
end
plot(plotC, plotM)
```

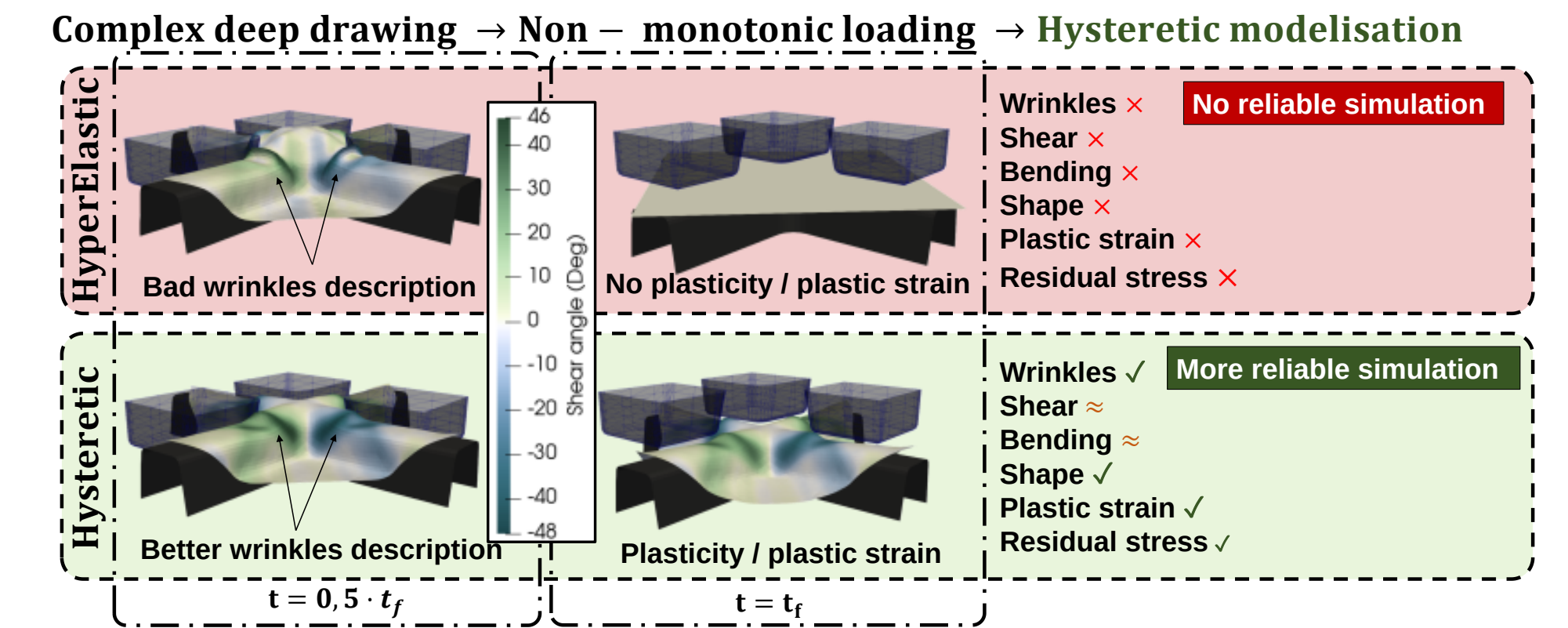
Complex deep drawing → Non − monotonic loading → Hysteretic modelisation
HyperElastic
Bad wrinkles description
No plasticity / plastic strain
Wrinkles ×
No reliable simulation
Shear ×
Bending ×
Shape ×
Plastic strain ×
Residual stress ×
Hysteretic
Better wrinkles description
Plasticity / plastic strain
Wrinkles ✓
More reliable simulation
Shear ≈
Bending ≈
Shape ✓
Plastic strain ✓
Residual stress ✓
Shear angle (Deg)
46
40
30
20
10
0
-10
-20
-30
-40
-48
t = 0,5 · t_f
t = t_f